INTEGRATED OPTICAL DISPLACEMENT SENSORS FOR SCANNING FORCE MICROSCOPIES

A THESIS
SUBMITTED TO THE DEPARTMENT OF PHYSICS
AND THE INSTITUTE OF ENGINEERING AND SCIENCE
OF BİLKENT UNIVERSITY
IN PARTIAL FULFILLMENT OF THE REQUIREMENTS
FOR THE DEGREE OF
MASTER OF SCIENCE

By
Coşkun Kocabaş
July 2003

I certify that I have read this thesis and that in my opinion it is fully adequate, in scope and in quality, as a dissertation for the degree of Master of Science.

Prof. Atilla Aydınlı (Supervisor)

I certify that I have read this thesis and that in my opinion it is fully adequate, in scope and in quality, as a dissertation for the degree of Master of Science.

Assoc. Prof. Recai Ellialtıoğlu

I certify that I have read this thesis and that in my opinion it is fully adequate, in scope and in quality, as a dissertation for the degree of Master of Science.

Prof. Hüseyin Zafer Durusoy

Approved for the Institute of Engineering and Science:

Prof. Mehmet Baray,
Director of Institute of Engineering and Science

Abstract

INTEGRATED OPTICAL DISPLACEMENT SENSORS FOR SCANNING FORCE MICROSCOPIES

Coşkun Kocabaş
M. S. in Physics
Supervisor: Prof. Atilla Aydınlı
July 2003

In this thesis, we have studied the use of integrated optical waveguide devices acting as integrated displacement sensors on cantilevers for scanning probe microscopes. These displacement sensors include integrated optical waveguide devices such as Bragg gratings, ring resonators, race track resonators and waveguide Michelson interferometers fabricated on a cantilever to measure the displacement of the cantilever tip due to the forces between surface and the tip. The displacement of the cantilever tip is measured directly from the change of the transmission characteristics of the optical device. As the cantilever tip displaces, the stress on the cantilever surface changes the refractive index of the materials that make up the integrated optical device which cause variations in its optical transmission characteristics. We have also studied an optical waveguide grating coupler fabricated on the cantilever for the same purpose. In two different embodiments of this device, light is either coupled in or out of the waveguide via the waveguide grating coupler. The displacement of the cantilever alters the direction of the scattered light and measuring the power of the scattered light with a position sensitive detector allows for the detection of cantilever

tip displacement. The novel design proposed in this work provides very high displacement sensitivity of the order of $10^{-4}\mathring{A}^{-1}$.

Keywords: Scanning Probe Microscopy, Scanning Force Microscopy, Mach-Zehnder interferometer, Ring resonator, Grating coupler, Displacement sensor, Integrated optics, Waveguide sensors.

Özet

TARAMALI UÇ MİKROSKOPLARI İÇİN TÜMLEŞİK OPTİK ALGILAYICILAR

Coşkun Kocabaş
Fizik Yüksek Lisans
Tez Yöneticisi: Prof. Atilla Aydınlı
Temmuz 2003

Bu tezde, tümleşik optik ışık kılavuzu aygıtlarının taramalı uç mikroskoplarında algılayıcı olarak kullanılması incelendi. Bragg kırınım ağı, halka çınlacı, Mach-Zehnder girişim ölçerinden oluşan bu algılayıcılar düzlemsel yay üzerine imal edilip yüzey ve iğne arasında oluşan kuvvet nedeniyle sapmasını ölçmek için kullanılmaktadır. Düzlemsel yayın sapması, üzerine monte edilmiş optik aygıtın ışık geçirgenliğindeki değişimden faydalanılarak ölçülmektedir. Düzlemsel yaya takılı olan iğnenin haraketi sırasında düzlemsel yayın yüzeyinde oluşan zor, optik aygıtın kırınım indisini değiştirmesi sonucu optik geçirgenlikteki değişimlere sebep olmaktadır. Benzer şekilde optik dalga kılavuzu kırınım ağı çifleyicileri de algılayıcı olarak kullanılmıştır. Bu aygıtlar içeri ve dışarı çifleyici olmak üzere iki farklı durumda incelenmistir. Düzlemsel yayın sapması sonucu saçılan ışığın doğrultusunda değişmeler oluşmakta ve saçılan ışığın şiddeti konum duyarlı fotodetektör ile ölçülebilmektedir. Önerilen bu yeni tasarım sayesinde $10^{-4}\mathring{A}^{-1}$ seviyesinde duyarlılık elde etmek mümkündür.

Anahtar sözcükler: Taramalı uç mikroskobu, Taramalı kuvvet mikroskobu, Mach-Zehnder girişim, Halka çınlacı, Kırınım ağı çifleyici, Tumleşik optik, Dalga kılavuzu algılayıcıları .

Acknowledgement

I would like to express my deepest gratitude to ***Prof. Atılla Aydınlı*** for his guidance, moral support, friendship and assistance during this research.

I would also like to thank to Prof. A. Oral and Prof. Nadir Dağlı from whom I have learned a lot.

I would like to thank my twin brother Aşkın for his help that has been invaluable for me.

I would like to thank İsa Kiyat for his help during this work especially analysis of ring resonator.

I would like to thank Mehrdad Atabak from whom I have learned the principles of AFM.

I would like to thank to all Integrated Optics Group members Feridun Ay, İsa Kiyat, Aşkın Kocabaş, Selcen Aytekin , İmran Akça and Nuh Sadi Yüksek for their friendship and to keep my sprits high.

Ertuğrul Çubukçu, Engin Durgun, Deniz Çakir, Cem Sevik, Turgut Tut, Sinem Binicioğlu, Ercan Avcı, Mustafa Kesir, Süleyman Tek, Necmi Bıyıklı helped to keep my spirits high all the time which I appreciate very much.

I am indebted to my family for their continuous support and care.

Contents

List of Figures

List of Tables

Chapter 1

Introduction

1.1 Scanning Probe Microscopy

Scanning probe microscope (SPM) is an instrument that measures the spatial variation of the local properties of a surface. SPM is a very powerful tool to produce highly detailed three dimensional images of a surfaces. Not only the topographic image but also other images of physical properties such as friction forces, temperature, magnetic field, electric field and charge of the surface can be determined using different configurations of the SPM.

The most important parameter for a microscope is the resolution. Resolution (or strictly speaking resolving power) is defined as the closest spacing of two points which can be resolved by a microscope to be separate entities. The resolution of conventional optical microscopes are limited by the diffraction of light and is typically of the order of a micrometer. In the 1930s, electron microscopes were developed which uses an electron beam instead of light rays and nanometer order resolution was obtained. However, the atomic scale resolution was still impossible. In 1982 Gerd Binning and Heinrich Rohrer [1] invented the scanning tunnelling microscope (STM) and they achieved atomic resolution and they were awarded the Nobel Price. Invention of STM has stimulated the development of more than two dozen types of SPMs. Atomic force microscope (AFM) [2] , lateral force microscope (LFM) [3] , magnetic force microscopes (MFM) [4] , near field

scanning optical microscope (NSOM) [5] are some of the different aspects of the SPM.

The main principles of the scanning force microscopes are similar, a sharp pyramidal tip mounted on a cantilever is brought close proximity to the surface and attractive or repulsive forces between the surface and the sharp tip causes the cantilever to bend. Monitoring the bending of the cantilever, it is possible to determine the image of the surface. The key component of the force microscope is a cantilever with the tip. The tip must be sharp enough to achieve high resolution and the cantilever must have appropriate properties for the type of operation selected. Three types of operations are most commonly used: 1) contact mode, the tip contacts with the surface and the force constant of the cantilever has to be low enough to avoid the damage on the sample, 2) non-contact mode, the tip is brought in close in proximity of the surface and vibrates near its resonant frequency, for which large force constant cantilevers are preferred and 3) intermittent contact mode, here the cantilever vibrates with its resonant frequency and the tip periodically touches the surface for which cantilevers with high force constant are preferred [6].

1.2 Displacement Sensors for SPM

Many scanning probe microscopies require the measurement of the displacement of the cantilever with high sensitivity. A good example is scanning force microscope [2] , based upon the principle of sensing the forces between a tip and a surface. These forces induce the displacement of the tip mounted on the cantilever. There is a great need to determine the displacement of the cantilever with high sensitivity to work out the attractive and repulsive forces between surface and the tip. There are many different deflection sensing systems to determine the cantilever deflection. These systems can be categorized into two main groups; external and integrated deflection detection systems. All these systems have advantages and disadvantages over each other. In this chapter, some of these systems will be discussed briefly. There are many other methods

and the detailed information can be found in the reference cited [7] .

1.2.1 External Deflection Sensing Systems

External detection systems use external physical components to measure the deflection of the cantilevers. In this section, principles advantages and disadvantages of some of these methods will be discussed. External systems are commonly used due to their high sensitivity, however these techniques require the use of precisely aligned optical components which limits the surface area and they are not very suitable for UHV environment due to their complexity.

Optical Lever Detection

Most widely used technique is the optical lever technique [8,9] . In this technique, an external collimated laser light is reflected from the cantilever surface and detected with a position sensitive detector (PSD). PSD is placed at a large distance from the cantilever. A differential amplifier is used with the PSD. As the cantilever deflects, the intensity of the light falling on the detectors differs and by monitoring the output of the differential amplifier, which is a linear function of the cantilever displacement, it is possible to detect the displacement. The resolution of this method is about 0.1 $\mathring{A}$. Although this method is very simple and cheap, it has low sensitivity and requires alignment during the surface scan and it is not very suitable for cantilever arrays.

Interferometric Detection

A highly sensitive technique is the interferometric detection which uses a cleaved end of an optical fiber and the back side of the cantilever as a Fabry-Perot interferometer [10–12] . As the cantilever displaces, the spacing between the fiber and cantilever surface differs and the reflection spectrum of the Fabry-Perot changes. The reflected light produces a photocurrent on the photo-detector and this photocurrent is used to image the force acting on the tip. Using this technique, it is possible to achieve $\pm$ 0.01$\mathring{A}$ resolution, however, it requires

accurately positioning the fiber to the cantilever and keeping the alignment during the surface scan which limits the scan area and this method is also not suitable for cantilever arrays.

Tunnelling Detection

This method was firstly used by Binning *et. al.* [2] Tunnelling detection method uses the tunnelling of the electrons from the conducting cantilever to the conducting tip. The application of the bias voltage between tip and cantilever produces a tunnelling current though the air gap. Tunnelling current exponentially decreases with the tip-cantilever separation. Tip-cantilever separation is about several angstroms. As the cantilever displaces, the tunnelling current decreases, and by monitoring the tunnelling current it is possible to determine the cantilever displacement.

Interdigital Detection

A further method is to use two sets of interdigitated fingers [13,14] , one reference set being attached to the substrate from which the cantilever extends and the other movable set being attached to the tip of the cantilever. The interdigitated fingers form an optical phase grating. The deflection of the cantilever is measured by directing a light beam onto the optical phase grating and measuring the diffracted light in reflection. This method provides the highest sensitivity up to date, $\pm$ 0.002 $\mathring{A}$ resolution is possible however, it requires alignment of laser beam and also the photo-detector. This method was also demonstrated for 5×1 cantilever arrays.

1.2.2 Integrated Deflection Sensing Systems

Integrated deflection sensing systems use an integrated sensor on a cantilever and measure the changes in a physical property of the sensor due to the bending of the cantilever. These sensors are very compact and they are individually addressable which allows them to be used in cantilever arrays. The main problem

of the integrated sensors is their sensitivity. They generally have two orders of magnitude less sensitivity than the external sensors. There is still the need to have highly sensitive integrated sensors.

Piezo-resistive Sensors

This method was firstly introduced by Tortonese *et. al.* [6] in 1991. Piezoresistive effect was used for sensing mechanism. The variation of resistivity with applied stress is known as piezoresistive effect. A piezoresistive element integrated on the cantilever is used to sense the generated stress on the surface due to the bending of the cantilever. This method is very compact and it does not require any alignment and also it is suitable for cantilever arrays, but it has three orders of magnitude less sensitivity than the other methods.

Piezoelectric Sensors

In this method [16], a cantilever made up of piezoelectric material, such as lead zirconate titanate (PZT), zinc oxide (ZnO), piezoelectric polymer (PVDF), is used , or piezoelectric film is sputtered on a cantilever and electrodes are made on the upper and lower surface. As the cantilever displaces, a voltage is generated between the electrodes due to piezoelectric effect. By measuring the generated voltage it is possible to determine the cantilever displacement. This method can also be used as an integrated actuator to control the cantilever displacement.

Integrated Transistor Sensors

An integrated MOS transistor was used as a force sensor by Akiyama *et al.* [17] in 1998. When the channel of the MOS transistor is subjected to stress, the carrier mobility changes, resulting in a changing source-drain current. The MOS transistors and read out circuit can be fabricated with conventional CMOS process. The channel of the transistor is at the surface, where stress gets its maximum value, therefore the sensitivity of this sensor is slightly higher than the piezoresistive sensors.

Capacitive Sensors

This method uses the capacitive lever displacement detection [18, 19]. Force induced cantilever displacements yields capacitive changes by changing the electrode spacing. Compared to the other integrated sensors, this sensor has high sensitivity. Capacitive detection is also interesting because it is free of parasitic resistive noise.

1.3 Aim of This Study

The main goal of this thesis work is to design and analyze highly sensitive integrated optical waveguide sensors for scanning probe microscopes to measure cantilever displacement. It is another objective of this thesis work to provide displacement sensors compatible with cantilever arrays which are suitable for nano-lithography systems and data storage technology. The novel design proposed in this work provide displacement sensors which do not require any tedious alignment of laser. The advantage of the present sensors over the prior work is that they provide for simple and compact integrated optical waveguide displacement sensors that measure the cantilever displacement without any or little alignment.

Chapter 2

Theoretical Considerations

This chapter is devoted to theoretical background for the design of integrated optical displacement sensors. Formalism and the basic principles of the computational methods which will be extensively used during the next chapters will be studied.

2.1 Overview of the Integrated Optical Sensors

The fiber optic and integrated optic technologies for measurement systems is very attractive. The integrated optic (IO) sensors have many advantages over their electronic counterparts. The main advantage of IO sensors is that it is possible to fabricate several components on a single chip which provides very compact and stable systems. Guided wave structures are immune to electromagnetically active environments and they have higher sensitivity than the electronic sensors. Recently, there have been many studies on the IO pressure sensors, bio-sensors, temperature sensors and strain sensors. These sensors consist of integrated optical devices such as Mach-Zehnder interferometers [20] , Michelson interferometers [21] , Bragg gratings [22] , directional couplers [23] , and ring-resonators [24] , whose transmission characteristics change due to external effects. The integrated optic sensors mostly use the two beam interference structure. An external physical value to be measured induces a phase

shift between two guided beams and this phase shift produces intensity change at the output of the sensor. By monitoring the intensity changes the external physical value is measured.

In this thesis, we introduce integrated optical detection method for scanning force microscopies. In the first chapter, different detection mechanisms were discussed. Considering other detection methods, integrated optical method has many advantages over others. First, an integrated sensor does not require any alignment of the laser and detector during surface scanning and it is possible to scan large areas. Second, integrated sensors are suitable for cantilever arrays due to their compactness, simplicity and potential for mass production. Another important aspect of the integrated sensors is that they provide individually addressable operation. It should also be mentioned that integrated sensors such as piezo-resistive ones [6] have less sensitivity (about $10^{-7}\mathring{A}^{-1}$) than the external sensors such as optical levers [8] (about $10^{-5}\mathring{A}^{-1}$). Using an integrated optical sensor, we expect to achieve as high sensitivity as external sensors. Integrated optical devices can be inexpensive and they can be used in harsh environments such as UHV systems and electromagnetically active environments. Integrated optical method is based on the detection of the changes of the transmission characteristics of an integrated optical devices due to the deflection of the cantilever. We will apply different types of integrated optical devices for displacement detection. Basically, we can categorize these devices into two groups: in the first group, transmission characteristics of the optical device, which is integrated on the cantilever, changes due to the photo-elastic effect and elongation of the optical path, in the second group the transmission characteristics changes due to the change of the coupling efficiency which alters the transmission of the optical device. In this chapter, theoretical background and formalism will be given and in the next chapters analysis of different types of integrated optical devices such as, Mach-Zehnder interferometer, Michelson interferometer, micro-ring resonator, Bragg grating and grating input and output coupler will be discussed thoroughly.

2.2 Design of the Waveguide Structures

Waveguide structures are the central part of the integrated optical devices. Detailed analysis of waveguide structures can be found in the references cited [25, 26] . In this section basic principles of the waveguide structures and the design for the sensor application will be discussed. Basically, thin films deposited on a dielectric substrate are used as optical waveguide if the film refractive index is higher than the substrate index. Basic waveguide structures are given in the Figure 2. 1. The simplest optical waveguide structure is the step-index slab waveguide. The slab waveguide consists of a high index dielectric layer surrounded with low index dielectric layers. The guiding layer has a finite thickness in the x direction and infinite in yz plane which is shown in Fig. 2. 2. In order to achieve total internal reflection in the guiding layer, the index of refraction of the substrate and the cover layer must be smaller than the guiding layer. If the cover and the substrate materials have the same index of refraction, this waveguide is called a symmetric, otherwise it is called an asymmetric waveguide. The electromagnetic analysis of the optical waveguide structures

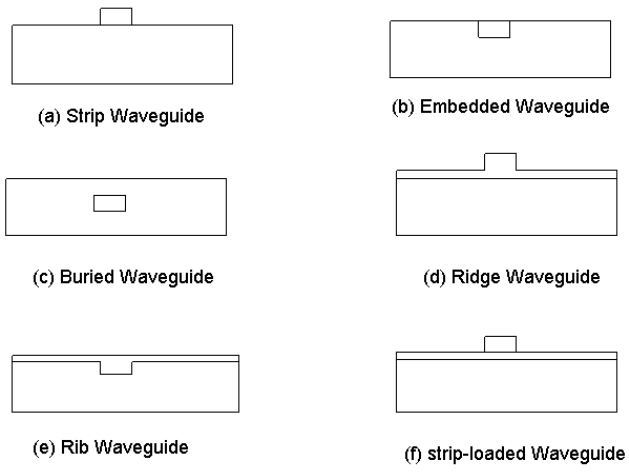

Figure 2. 1: Different types of optical waveguides

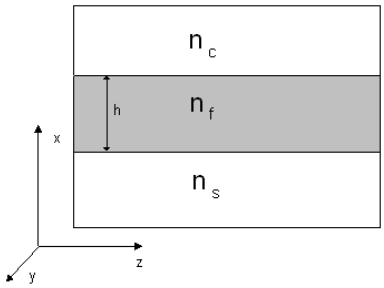

Figure 2. 2: Schematics of slab waveguide with refractive index of n_f, n_s, n_c for film, substrate and cover, respectively

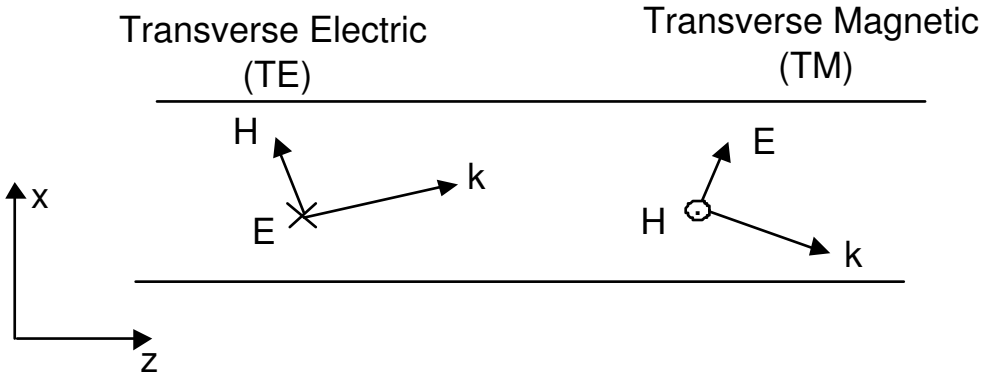

Figure 2. 3: Directions of electric and magnetic for Transverse Electric (TE) and Transverse Magnetic (TM) polarization

are based on the solving the Maxwell equations using the suitable boundary conditions. The solution of the Maxwell equations gives the specific propagation direction and the electromagnetic field distributions which is called *modes* of the waveguide. Consider an asymmetric waveguide such that $n_f > n_s > n_c$ with the guiding layer thickness of h. During the analysis we choose z as the propagation direction and x as the normal direction of the waveguide plane. For slab waveguide, rectangular coordinate system is the most suitable coordinate system because the electromagnetic fields can be uncoupled to E_x, E_y and E_z which simplifies the analytic solution. The orientation of the electric fields have two different polarizations, *transverse electric* (TE) and *transverse magnetics* (TM). Figure 2. 3 depicts the two different polarizations for slap waveguide.

First, we will solve wave equation for TE polarization and the solution for the TM polarization is similar when the electric fields are replaced with magnetic fields. For TE polarization E field is polarized along the y direction and the light source which excite the waveguide has the frequency of w_0. In order to find the allowed modes for the waveguide, wave equation must be solved for each layer and they must be combined with the boundary conditions. The wave equation for electromagnetic waves in a dielectric medium can be written as

$$\nabla^2 E_i - \mu\varepsilon \frac{\partial^2 E_i}{\partial t^2} = 0 \tag{2. 1}$$

Here the subscription refers to the i^{th} component. To find the solution, we have to use the separation of variables techniques in cartesian coordinate system and we get the scalar wave equation for each component and we expect the trial solution as

$$E_y(x, z, t) = E_y e^{-j\beta_i z} e^{jw_0 t} \tag{2. 2}$$

where β_i is the propagation coefficient along the z direction. Inserting the trial solution into the Eq. 2. 1, we get

$$\frac{\partial^2 E_y}{\partial x^2} + (k_0^2 n_i^2 - \beta^2) E_y = 0 \tag{2. 3}$$

We have to solve this equation for three layers with the refractive indices n_s, n_c, n_f. From the Eq. 2. 3 we get the transverse field amplitude in the exponential form. Two cases must be considered, i) $\beta > k_0 n_i$ and ii) $\beta < k_0 n_i$. For $\beta > k_0 n_i$ transverse field amplitude, which is called the *evanescent field*, is

$$E_y = E_0 e^{\pm\sqrt{\beta^2 - k_0^2 n_i^2}} \tag{2. 4}$$

and for $\beta < k_0 n_i$

$$E_y = E_0 e^{\pm j\sqrt{k_0^2 n_i^2 - \beta^2}} \tag{2. 5}$$

which is an oscillating field. Our aim is to find the allowed β values. In order to do this we should write the field amplitudes for three layers and matching them at the boundaries considering the continuity of the tangential electric and

magnetic fields. The field amplitudes for three layers are

$$\begin{aligned} E_y(x) &= Ae^{-\gamma_c x} \quad 0 < x \\ E_y(x) &= Bcos(\kappa x) + Csin(\kappa x) \quad -h < x < 0 \\ E_y(x) &= De^{\gamma_s x} \quad x < -h \end{aligned} \tag{2. 6}$$

where A,B,C,D are the coefficients to be determined. Applying the boundary conditions at the two interfaces, we get a transcendental equation for β,

$$tan(h\kappa_f) = \frac{\gamma_c + \gamma_s}{\kappa_f(1 - \frac{\gamma_c\gamma_s}{\kappa_f^2})} \tag{2. 7}$$

here $\gamma = \sqrt{\beta^2 - k_0^2 n_i^2}$ and $\kappa = \sqrt{k_0^2 n_i^2 - \beta^2}$. The solution of the Eq. 2. 7 gives discrete values of β. The physical meaning of β is the component of the wavevector along the propagation direction. This means that the guided light propagates at certain angles along the z direction.

2.3 Beam Propagation Method

In the previous section we have defined the fundamentals of the optical waveguides. In this section we will describe the numerical solutions for more complicated structures using Beam Propagation Method (BPM). BPM is the most widely used propagation technique for modelling the integrated and fiber optic photonic devices. For device simulation we have used commercial software package BeamPROP [27]. In the BPM the exact wave equation is approximated for monochromatic waves and it is solved numerically. By neglecting the polarization of the wave, we get a three-dimensional scalar wave equation (Helmholtz Equation) which is the fundamental equation to be solved by BPM. The scalar wave equation is written as

$$\frac{\partial^2 E}{\partial x^2} + \frac{\partial^2 E}{\partial y^2} + \frac{\partial^2 E}{\partial z^2} + k^2 n(x,y,z)^2 = 0 \tag{2. 8}$$

Electric field can be separated in two parts; the envelope term $\Phi(x, y, z)$ which is a slowly varying function and the rapidly varying term e^{-jkn_0z} where z is the propagation direction. Another approximation is the weakly guiding approximation $(n^2 - n_0^2) = 2n_0(n - n_0)$. Substituting these in to the Eq.2. 8 we get

$$\frac{\partial \Phi}{\partial z} = -j\frac{1}{2kn_0}\nabla^2\Phi - jk(n - n_0)\Phi \qquad (2.\ 9)$$

This equation is solved by standard numerical techniques. Firstly Φ is defined only as discrete points on a grid. Differentiation is defined as finite differential and the goal is to derive the numerical equation that determines the fields at the next z plane. Gaussian launch field is taken as initial field at the initial z plane and using the numerical equation the field is propagated along the z direction. BPM provides accurate results under certain conditions. These conditions are that, the refractive index of the device must be slowly varying function of z and the propagation is restricted to a narrow range of angles. S-shaped bend waveguides, tapered waveguides, directional couplers, branching and combining waveguides can be simulated. Also the modes of a waveguide (field distributions) can be obtained. Fig.2. 4 illustrates the electric field distribution of an $GaAlAs/GaAs$ waveguide structure obtained from BPM. More detailed information can be found in the references cited [28].

2.4 Photo-elastic Effect

Photo-elastic effect is the change in the refractive index of a material under applied stress. This phenomenon was first discovered by Sir David Brewster in 1815 and systematically investigated by Pockel. During the investigation of the photo-elastic effect, formalism of *index ellipsoid* plays the central part. Index ellipsoid defines an ellipse in which the distance from the origin to the surface of the ellipsoid represents the magnitude of the refractive index of the crystal in any direction. Figure 2. 5 represents the index ellipsoid where k is the wavevector and $x^{'}, y^{'}, z^{'}$ represents the principle directions in the crystal. Equation for the

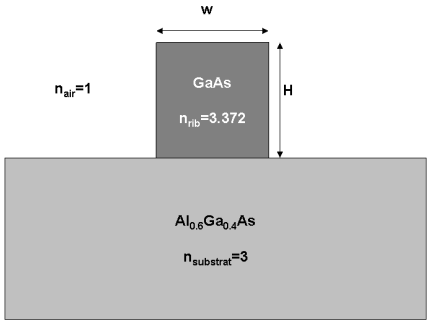

(a)

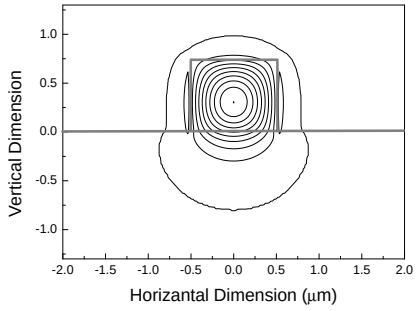

(b)

Figure 2. 4: (a)Geometry of the waveguide and (b) electric field distribution of single mode $GaAlAs/GaAs$ waveguide. $n_{GaAlAs} = 3.00, n_{GaAs} = 3.37$

ellipsoid can be written as

$$\frac{x'^2}{n_x^2} + \frac{y'^2}{n_y^2} + \frac{z'^2}{n_z^2} = 1 \tag{2. 10}$$

If a wave propagates in k direction, the effective index for the wave depends on the polarization of the electric fields, and it lies in the circle shown in the Figure 2. 5. When external stress applied on the material, the dielectric tensor $(\frac{1}{n^2})$ is transformed like a second rank tensor and it can be written as

$$\Delta(\frac{1}{n^2})_i = \sum_{j=1}^{6} p_{i,j} S_j \tag{2. 11}$$

where $p_{i,j}$ represents the strain optic coefficients and S_j represents the present strain. Here $i = 1, 2, ...6$ represent the strain components xx, yy, zz, yz, zx, xy,

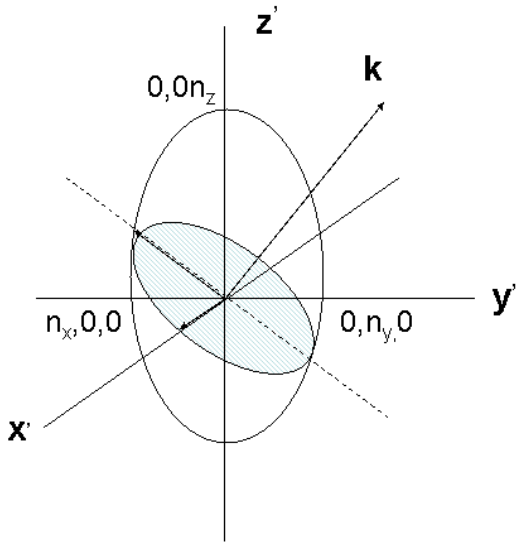

Figure 2. 5: Index ellipsoid and propagation direction of a wave

respectively. From Eq. 2. 11 we can get

$$\Delta n = \frac{-n^3}{2} \sum_{j=1}^{6} p_{i,j} S_j \tag{2. 12}$$

Strain can also be written in terms of the stress components and we can write Eq.2. 12 in terms of the stress and we get

$$\Delta n_i = \sum_{j=1}^{6} C_{j,i} \sigma_j \tag{2. 13}$$

where $C_{j,i}$ are the photo-elastic coefficients and σ_i are components of the stress. For isotropic medium $C_{j,i}$ have two different values; longitudinal photo-elastic constant C_L and transverse photo-elastic constant C_T. Using these constants, we can write refractive index changes for each direction as,

$$\Delta n_x = C_L \sigma_x + C_T(\sigma_y + \sigma_z) \tag{2. 14}$$

$$\Delta n_y = C_L \sigma_y + C_T(\sigma_x + \sigma_z) \tag{2. 15}$$

	$GaAs$	Si	SiO_2	Si_3N_4
C_L (Pa^{-1})	$1.7\ 10^{-11}$	$1.56\ 10^{-11}$	$-0.75\ 10^{-12}$	$-5.3\ 10^{-12}$
C_T (Pa^{-1})	$1.0\ 10^{-11}$	$-0.45\ 10^{-11}$	$-4.1\ 10^{-12}$	$-1.8\ 10^{-12}$

Table 2.1: Stress optic coefficients for waveguide materials.

$$\Delta n_z = C_L \sigma_z + C_T(\sigma_y + \sigma_x) \tag{2. 16}$$

C_L and C_T can be written as

$$C_L = \frac{-n^3}{2E}(p_{11} - 2\nu p_{12}) \tag{2. 17}$$

$$C_T = \frac{-n^3}{2E}(-\nu p_{11} + (1-\nu)p_{12}) \tag{2. 18}$$

where p_{11} and p_{12} are the strain optical coefficient, n is the refractive index, E is the Young's Modulus and ν is the Poisson ratio of the material. We can make an analogy between the photo-elastic effect and the electro-optic effect. They both deform and rotate the index ellipsoid, but whereas photo-elastic effect is universal and it can be observed in symmetric and asymmetric crystals such as Si and GaAs, electro-optic effect can only be observed in asymmetric crystals (without inversion symmetry) such as GaAs (not Si). Quadratic electro-optic effect (Kerr effect) is also universal like as photo-elastic effect [29]. In Table 2.1 we summarize the stress optic coefficients for different materials. GaAs and Si have large stress optic coefficients.

2.5 Finite Element Method Analysis

Finite Element Method (FEM) was firstly developed for the stiffness analysis of airplanes. Stress analysis is the most common application of FEM. There are many formulations that are used to solve FEM problems. Two of them are minimum total potential energy formulation, weighted residual formulation . We have used total potential energy formulation (TPEF). TPEF is the common

method for solid mechanics. When the external forces applied on a structure, structure deforms and the work done by the external forces is stored as elastic energy (strain energy). Deformation of the solid (displacement) can be written as

$$\vec{\delta} = u(x,y,z)\hat{i} + v(x,y,z)\hat{j} + w(x,y,z)\hat{k} \tag{2. 19}$$

Strain vector has six components and can be written from the displacement as

$$\begin{aligned} \varepsilon_{xx} &= \frac{\partial u}{\partial x} \\ \varepsilon_{yy} &= \frac{\partial v}{\partial y} \\ \varepsilon_{zz} &= \frac{\partial w}{\partial z} \\ \gamma_{xy} &= \frac{\partial u}{\partial y} + \frac{\partial v}{\partial x} \\ \gamma_{yz} &= \frac{\partial v}{\partial z} + \frac{\partial w}{\partial y} \\ \gamma_{xz} &= \frac{\partial u}{\partial z} + \frac{\partial w}{\partial x} \end{aligned} \tag{2. 20}$$

For elastic materials there is a relationship between stress and strain according to the Hooke's Law and given by the following equation

$$\begin{aligned} \varepsilon_{xx} &= \frac{1}{E}[\sigma_{xx} - \upsilon(\sigma_{yy} - \sigma_{zz})] \\ \varepsilon_{yy} &= \frac{1}{E}[\sigma_{yy} - \upsilon(\sigma_{xx} - \sigma_{zz})] \\ \varepsilon_{zz} &= \frac{1}{E}[\sigma_{zz} - \upsilon(\sigma_{xx} - \sigma_{yy})] \\ \gamma_{xy} &= \frac{1}{G}\tau_{xy} \\ \gamma_{yz} &= \frac{1}{G}\tau_{yz} \\ \gamma_{zx} &= \frac{1}{G}\tau_{zx} \end{aligned} \tag{2. 21}$$

where E is the Young's modulus and G is the shear modulus. Potential energy can be written as

$$(strainenergy) = \frac{1}{2}\int (stress)^T (strain) dV \qquad (2.\ 22)$$

The main goal is to minimize this integral equation. Structure is firstly discretized into small elements and the solution of the problem is approximated in each element with suitable shape functions and the unknown constant (to be determined) at the nodal points. Applying this approximation and minimizing the integral by taking the derivative for each unknown constant, the entire problem is reduced to a matrix equation. The most important thing that has to be considered is the shape function and the element shape. More detailed information can be found in the references cited [26, 31].

2.5.1 Cantilever Design

Fundamental mechanical parameters of an AFM cantilever are its spring constant and resonant frequency. The optimal values of these parameters depend on the mode of the operations, namely contact mode, non-contact mode, and intermittent contact mode. $GaAs$ has a large photo-elastic constant which makes it a suitable material for fabrication of integrated optical devices and cantilever. Other materials such as Si_3N_4 and Si can also be used with varying sensitivities. Our design is based on rectangular cantilevers which are compatible with well established micromechanical fabrication technology. For a rectangular cantilever, spring constant and resonant frequency can be written as,

$$k = \frac{Ewt^3}{4l^3} \qquad (2.\ 23)$$

and

$$f_0 = \frac{t}{l^2}(\frac{E}{\rho})^{1/2} \qquad (2.\ 24)$$

respectively. Here E is the Young's modulus, ρ is the density of the cantilever material and t is the thickness, l is the length, w is the width of the cantilever. Typical micromachined cantilevers for AFM have lengths of 100 μm to 400 μm,

	$GaAs$	Si	SiO_2	Si_3N_4
$Young's Modulus\ (GPa)$	85	130	75	$85-105$
$Poisson\ Ratio$	0.31	0.279	0.17	0.24

Table 2.2: Mechanical properties of some materials.

widths of 20 μm to 50 μm and thicknesses of 0.4 μm to 10 μm. A large spring constant is preferable for non-contact mode and intermittent mode operations. On the other hand, low force constant is preferable for contact mode operations. The resonant frequency is required to be a few kHz in order to minimize the external effects [48]. During the analysis we choose a rectangular cantilever length of 200 μm width of 50μm and thickness of 5 μm. The resonance frequency is 50 kHz, the spring constant is 16 N/m. In Table 2.2, mechanical properties of different materials are summarized.

2.5.2 Finite Element Method Stress Analysis of the Cantilever

In any cantilever design, the measurement of the displacement of the cantilever with high sensitivity is the essential task. The design of the cantilever and the type of the integrated sensor plays a fundamental role to increase the sensitivity. Bending the cantilever generates stress which is the necessary physical quantity used to characterize the displacement of the cantilever. Photo-elastic effect is used for the sensing mechanism; stress generated on the cantilever changes the refractive index of the waveguide where the optical sensor is loaded. Furthermore, sensing the generated stress using integrated optical devices requires materials suitable for such devices with large stress optic coefficients. A good candidate is GaAs. Applying mechanical stress to GaAs results in variation of local index due to photo-elastic effect, therefore we will use GaAs as a cantilever material. Since the displacement of the tip causes mechanical stress along the cantilever, maximizing the stress on the sensing element will maximize the performance. Obtaining the generated stress is the essential task. The stress distribution on the rectangular cantilever can be written analytically. As the cantilever bends,

stress reaches its maximum value at the supporting point and decreases linearly along the cantilever. Therefore, the sensing element is placed at the supporting point where

$$\sigma_{max} = \frac{3Et}{2l^2} z \qquad (2.\ 25)$$

in which, E is the Young's Modulus, t is the thickness, l is the length and z is the displacement of the cantilever. To obtain more accurate results for complicated geometries Finite Element Method (FEM) analysis is employed. We have used general purpose FEM software program ANSYS. FEM analysis consist of four steps of, drawing the structure, meshing, applying boundary condition, and solving the static equation. In Fig. 2. 6 these steps are illustrated. Fig. 2. 6a represent the cantilever with length of 200 μm, width of 50 μm and thickness of 5 μm. Cantilever is fixed to a substrate from one end and the other end is free. Fig. 2. 6 b represents the meshed geometry. The meshing has to be increased near the supporting point where the optical device will be placed. Fig. 2. 7 shows the stress distribution on the cantilever for 100 $\mathring{A}$ displacement. Longitudinal stress is much larger than the transverse stress and in our calculation we can neglect the transverse stress. Longitudinal stress reaches its maximum value (1.5 $10^5 Pa$) at the supporting point of the cantilever and decreases linearly along the cantilever. There is good agrement between the FEM results and the analytical expression for stress distribution.

2.6 Coupled Mode Theory

Coupled Mode Theory (CMT) will be used for the design of the grating to calculate the coupling coefficient. CMT describes how energy exchange occurs between two guided modes in an integrated optical device. There are much similarities between the perturbation theory in quantum mechanics and the CMT for integrated optics. In an ideal waveguide (no perturbation) the amplitude of a guided mode does not change along the waveguide. If there is a perturbation, the ideal mode starts to couple to other guided or radiative modes and the amplitude decreases. Consider a multi mode waveguide. For each mode transverse electric

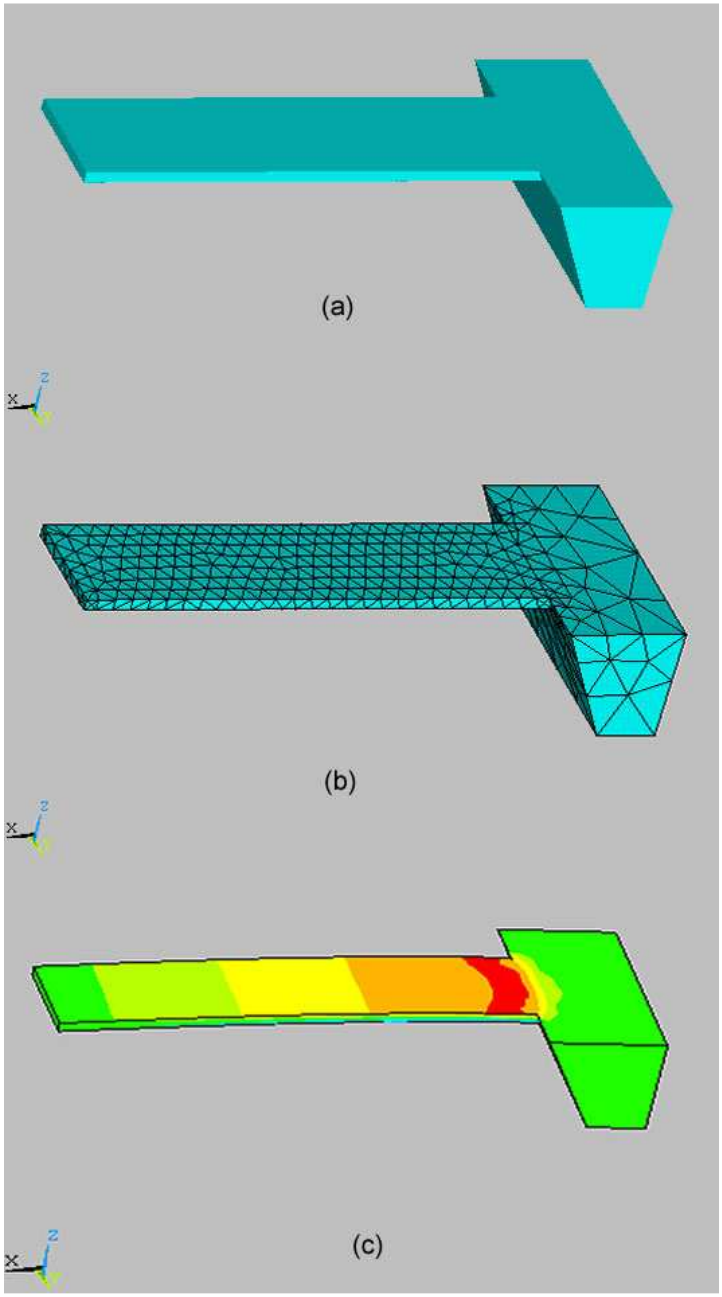

Figure 2. 6: (a) Cantilever structure, (b) meshed geometry, (c) stress distribution on the cantilever for 100 $\mathring{A}$ displacement.

field amplitude can be written as

$$E_{y_i}(x,z,t) = \frac{1}{2} A_i \xi_{y_i}(x) e^{-j(\beta_i z - \omega t)} + c.c. \qquad (2.\ 26)$$

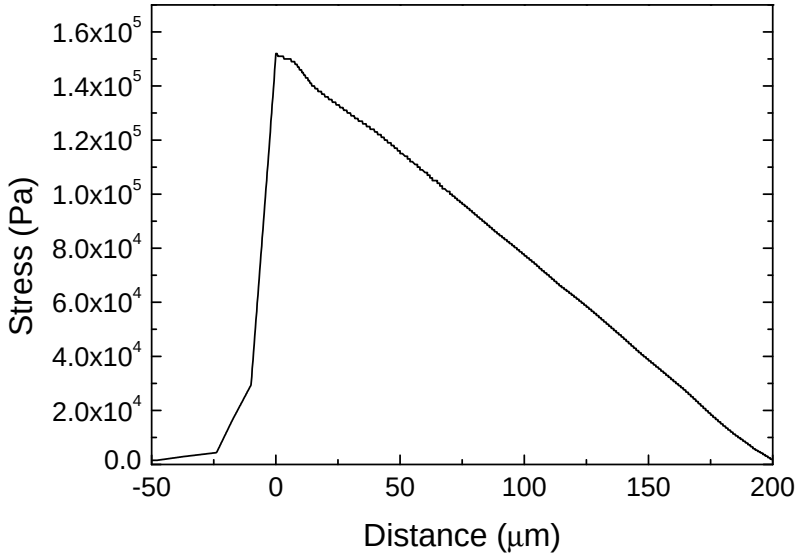

Figure 2. 7: Longitudinal stress distribution on the cantilever, stress reaches its maximum value at the supporting point of the cantilever and decreases linearly along the cantilever.

The subscription i represent different modes in the waveguide and A_i is the amplitude and $\xi_{y_i}(x)$ is the normalized amplitude for the modes. If there is no change in the dielectric constant (refractive index) or in the dimension along the waveguide, different modes do not couple each other, they are completely independent. If there is a perturbation, this makes the modes couple to each other and energy exchange starts. The perturbation can be in two different ways; refractive index may change along the waveguide or an electric field from a second source appears in the waveguide and it may excite the mode and the field amplitudes increases along the waveguide. Perturbation introduces an extra term in the electric flux. Electric flux for unperturbed condition can be written as

$$D = \epsilon E = \epsilon_0 E + P \tag{2. 27}$$

Where P is the polarization in the dielectric. The effect of the perturbation increases the electric flux and the electric flux is modified as

$$D = \epsilon E + P_{pert} \tag{2. 28}$$

if we substitute this equation into the wave equation we get

$$\nabla^2 E_y = \mu\epsilon \frac{\partial^2 E_y}{\partial t^2} + \mu \frac{\partial^2 P_{pert}}{\partial t^2} \tag{2. 29}$$

If we substitute Eq.2. 26 in to this equation and with simple algebra we can drive the famous mode coupling equation between the modes which propagates in positive and negative directions as

$$\frac{\partial A_i^+}{\partial z} e^{j(\beta z+\omega t)} - \frac{\partial A_i^-}{\partial z} e^{j(\beta z+\omega t)} + c.c. = \frac{-j}{2\omega} \frac{\partial^2}{\partial t} \int_{-\infty}^{\infty} P_{pert}(x).\xi_i(x) dx \tag{2. 30}$$

Where A_i^+ and A_i^- is the amplitudes for modes propagating in positive and negative directions. This is the fundamental equation that determines the contra-directional mode coupling. More advanced theories are being developed. Detailed analysis of CMT can be found in references cited [25, 26] .

2.7 Transfer Matrix Method

Spectral response of a Bragg grating can be calculated with Transfer Matrix Method (TMM) [30]. Surface corrugation introduces an effective index change and the grating structure can be modelled as a multilayered periodic structure. Figure 2. 8 represents a grating and its multilayered model. First, we study transmission and reflection from a single interface and we get a matrix relationship between the electric fields of the two medium. Then we will extend this concept to the periodic structure by multiplying the matrices for each layer. Figure 2. 9 shows a thin film with thickness of d and refractive index of n_2. The electric fields for three layers are written as

$$E = \begin{cases} \hat{y}E_1^+ e^{-jk_1 x} + \hat{y}E_1^- e^{jk_1 x} & x > 0 \\ \hat{y}E_2^+ e^{-jk_2 x} + \hat{y}E_2^- e^{jk_2 x} & 0 < x < d \\ \hat{y}E_3^+ e^{jk_3 d} e^{-jk_3 x} + \hat{y}E_3^- e^{-jk_3 d} e^{jk_3 x} & x > d \end{cases} \tag{2. 31}$$

where $k_i = \omega/c = k_0 n_i$ $i = 1, 2, 3$ and n_1, n_2, n_3 are the refractive index of each layer. And we can write magnetic field as

$$\vec{H} = \frac{1}{\omega\mu} \vec{k} \times \vec{E} \tag{2. 32}$$

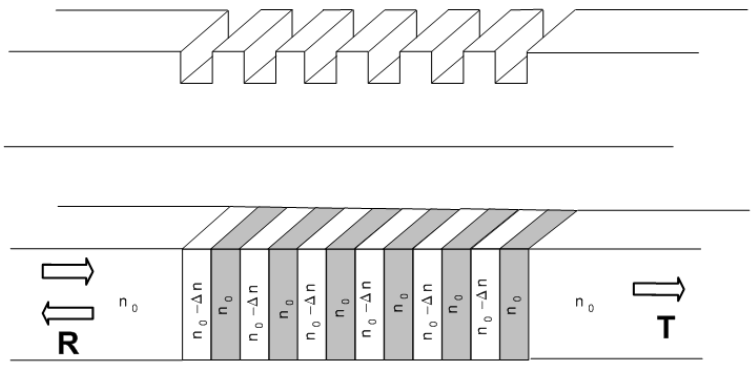

Figure 2. 8: Waveguide Bragg grating and its layer modelling

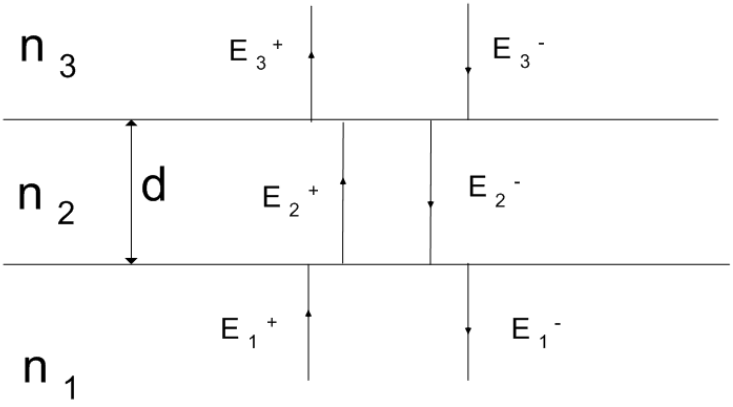

Figure 2. 9: Electric field for three layers with different refractive index

using the continuity of tangential electric and magnetic field components at the boundary,

$$E_1^+ + E_1^- = E_2^+ + E_2^- \tag{2. 33}$$

$$n_1(E_1^+ - E_1^-) = n_2(E_2^+ - E_2^-)$$

If we introduce matrix notation

$$\begin{pmatrix} E_1^+ \\ E_1^- \end{pmatrix} = S_1 \begin{pmatrix} E_2^+ \\ E_2^+ \end{pmatrix} = \frac{1}{t_1} \begin{pmatrix} 1 & r_1 \\ r_1 & 1 \end{pmatrix} \begin{pmatrix} E_2^+ \\ E_2^- \end{pmatrix} \tag{2. 34}$$

here r_1 and t_1 are the reflection and transmission amplitudes. They can be written as

$$r_1 = \frac{n_1 - n_2}{n_1 + n_2} \tag{2. 35}$$

$$t_1 = \frac{2n_1}{n_1 + n_2} \tag{2. 36}$$

we can write the same equations for the second interface with an extra phase term and

$$\begin{pmatrix} E_2^+ \\ E_2^- \end{pmatrix} = S_2 \begin{pmatrix} E_3^+ \\ E_3^+ \end{pmatrix} = \frac{1}{t_1} \begin{pmatrix} e^{j\delta_2} & r_2 e^{j\delta_2} \\ r_2 e^{-j\delta_2} & e^{-j\delta_2} \end{pmatrix} \begin{pmatrix} E_3^+ \\ E_3^- \end{pmatrix} \tag{2. 37}$$

phase term is $\delta_2 = k_2 d = k_0 n_2 d_2$. We define the ratio of the E_3^+ and E_1^1 to the E_1^+ as $t = \frac{E_3^+}{E_1^+}$ and $r = \frac{E_1^-}{E_1^+}$. E_1^- is the amplitude of reflected light and E_3^+ is the amplitude of transmitted light. Transfer matrix can be written as $S = \begin{pmatrix} a & b \\ c & d \end{pmatrix}$ and we get $r = \frac{c}{a}$ and $t = \frac{1}{a}$. Transmission and reflection of the layer are the ratio of the transmitted power and reflected power to the incident power which is the square of electric field and

$$T = \frac{n_3}{n_1}|t|^2 \tag{2. 38}$$

$$R = |r|^2 \tag{2. 39}$$

It is obvious that if there is no absorbtion $R + T = 1$ should be satisfied. Matrix method can be extended to multilayered structures. The aim is to find the total transfer matrix by multiplying the transfer matrices for each layer

$$S_{Total} = \prod_{i=0}^{N} S_i \tag{2. 40}$$

and transmission of multilayered structure is obtained. This method is very suitable to calculate the spectral response of the Bragg grating.

Chapter 3

Mach-Zehnder Interferometers

In this chapter we will discuss the use of Mach-Zehnder interferometer (MZI) as a displacement sensor for scanning force microscope. Mach-Zehnder interferometer is integrated on a cantilever and this provides integrated optical interferometric displacement detection. In Section 3.1 theoretical basis and operational principles of MZI will be discussed. In Section 3.2 integration of the MZI with a cantilever will be discussed, transmission characteristics of MZI will be studied. In Section 3.3 waveguide design considerations will be given. In Section 3.4 sensitivity analysis of the sensor will be given. In Section 3.5 basic experimental setup will be proposed.

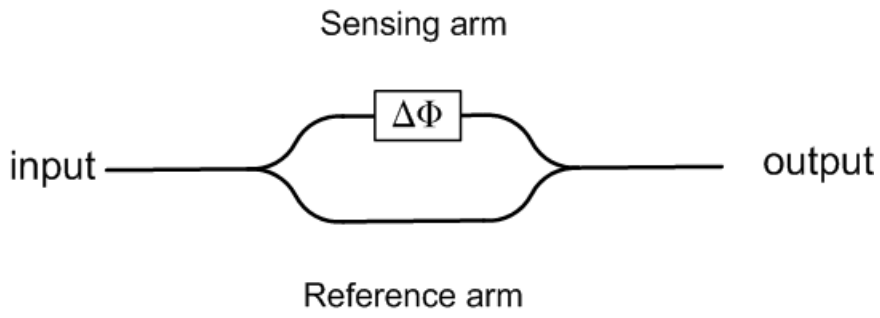

Figure 3. 1: Schematics of Mach-Zehnder interferometer

3.1 Physical Considerations

Mach-Zehnder interferometer (MZI) is one of the most commonly used integrated optical devices in sensor applications. MZI is based on the interference of two coherent beams. For a waveguide structure, guided light is split into two single mode waveguides by a 3-dB Y junction. Split beams travel different paths and then recombine at an other Y-junction. If the optical path lengths of the two arms differ, there exist a phase difference between the two guided beams and when they recombine, they interfere and the intensity of the light at the output port will change as a function of the phase shift and given as

$$I_{out} = \frac{I_0}{2}(1 + \cos(\Phi)) \tag{3. 1}$$

where I_0 is the input intensity and Φ is the phase shift between the two arms. When the phase shift is equal to π, the two beams interfere destructively and the output will be zero. Figure 3. 1 illustrate the MZI. For sensor applications one of the arms is used as a sensing arm and external physical value introduces optical path difference on the sensing arm leading to interference. For a pressure sensor, sensing arm is located on a suspended diaphragm. When the diaphragm is subject to an applied pressure, the diaphragm deflects and two simultaneous effects introduce phase shift on the sensing arm. The first effect is the photo-elastic effect, which changes the refractive index of the waveguide and the second

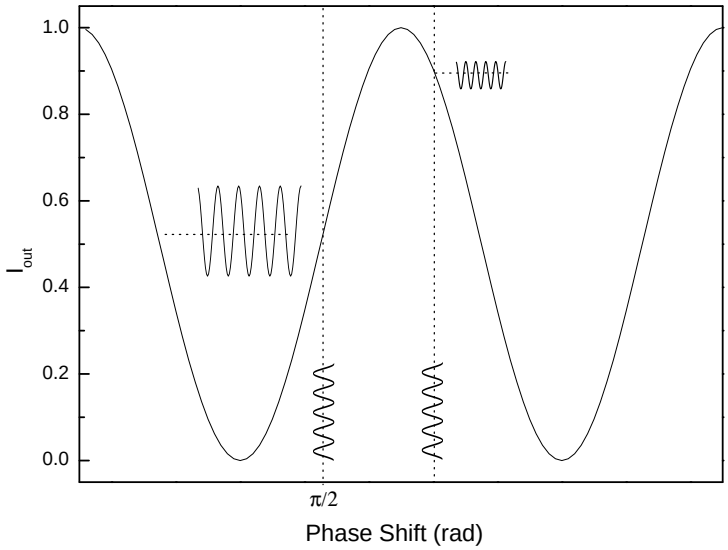

Figure 3. 2: Output intensity of Mach-Zehnder interferometer as a function of the phase shift. Small variation of the phase shift results in the output intensity variation, at the quadrature point ($\Phi = \pi/2$) maximum variation can be achieved

is the extension of the path length. The phase shift can be written by adding the two contributions as follows;

$$\Phi = \beta \Delta L + \int_L \delta\beta dL \tag{3. 2}$$

here β is the propagation constant of the single mode waveguide and it can be written as $\beta = n_{eff}\frac{2\pi}{\lambda}$, n_{eff} is the effective index of the waveguide, ΔL is the path elongation and $\delta\beta$ is the change of the propagation constant due to the photo-elastic effect. Fig. 3. 2 shows the output intensity variation as a function of the phase shift between the two arms. The sensitivity of the interferometer is defined as the output intensity variation per unit physical value such as pressure.

$$\frac{dI_{out}}{I_0 dP} = \sin\Phi \frac{d\Phi}{dP} \tag{3. 3}$$

where P is the applied applied physical value. Two things should be noted for Fig. 3. 2. First there is a very linear region between $\Phi = \pi/3$ and $\Phi = 2\pi/3$, secondly

this region has the steepest slope. Clearly, the maximum sensitivity occurs in this region with $\Phi = \frac{\pi}{2}$ where the slope of the output intensity is maximum and it is called *quadrature point*. In order to increase sensitivity MZI must be biased to quadrature point by introducing $\pi/2$ phase shift.

3.2 Mach-Zehnder Interferometer as a Displacement Sensor

The operational principle of the displacement sensor is simple, a single mode waveguide is divided into two arms with a Y-junction and one of the arm is placed on the cantilever and the other arm is placed on fixed side of the substrate and these two arms are combined with another Y-junction. Fig. 3. 3 represents the top view of the MZI integrated on the cantilever. As the the cantilever displaces, a phase shift is produced between the the two arms and the two beams interfere. As stated before, we can write the phase shift as

$$\Phi = \beta\Delta L + \int_L \delta\beta dL = \beta\Delta L + \int_L \Delta n_{eff}\frac{2\pi}{\lambda}dL \qquad (3.\ 4)$$

here there are two contributions; photo-elastic effect and path elongation. They can be additive or subtractive. If the cantilever bends in negative z direction optical path of the waveguide on the upper surface of the cantilever increases ($\Delta L > 0$) and stress is positive (tensile). On the other hand, change of refractive index under the tensile stress will be negative or positive depending on the value of the stress optic coefficient of the cantilever. Longitudinal stress optic coefficient for GaAs is positive. This means, under the tensile stress refractive index increases. For SiO_2, Si_3N_4 and Si longitudinal stress optic coefficient is negative and refractive index decreases under tensile stress. As a result $GaAs$ is the most suitable material for our purpose. Other materials may also be possible with varying sensitivities. As stated before, longitudinal stress is dominant and it decreases linearly along the cantilever and we can write

$$\sigma(x) = \sigma_{max}\frac{(L_{can} - x)}{L_{can}} \qquad (3.\ 5)$$

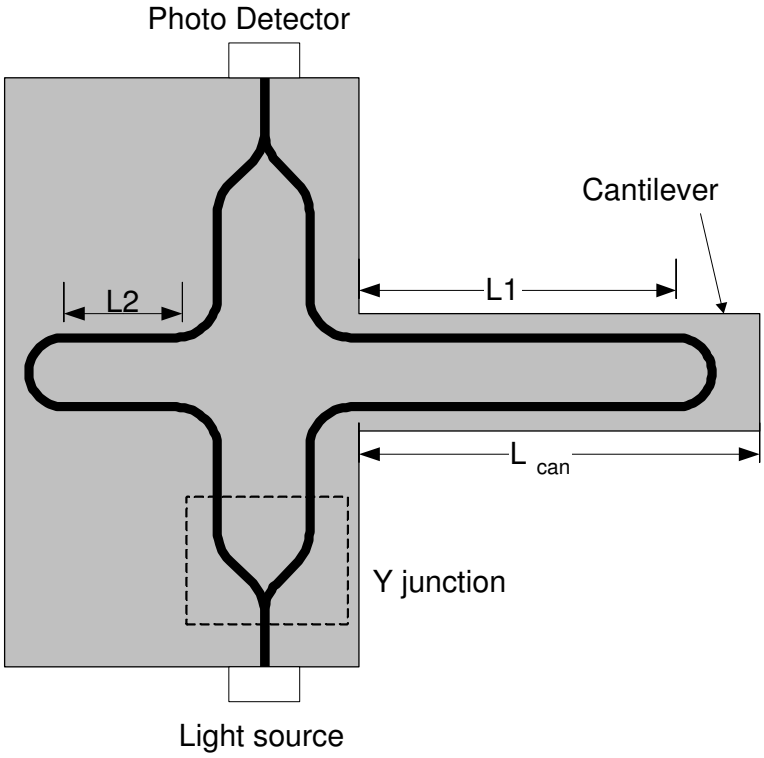

Figure 3. 3: Schematic of Mach-Zehnder interferometer integrated on a cantilever.

where L_{can} is the cantilever length and x is the distance from the supporting point. Using photo-elastic effect, index change can be written as

$$\Delta n_{eff} = C_T \sigma_{max} \frac{(L_{can} - x)}{L_{can}} \tag{3. 6}$$

Using FEM, we can calculate the stress distribution and the path elongation on the cantilever. Also an analytical expression can be written for maximum stress and inserting into Eq. 3. 4 we get

$$\Phi = \beta \Delta L + \frac{4\pi C_T \sigma_{max}}{\lambda} \int_0^{L_{MZI}} \frac{(L_{can} - x)}{L_{can}} dL \tag{3. 7}$$

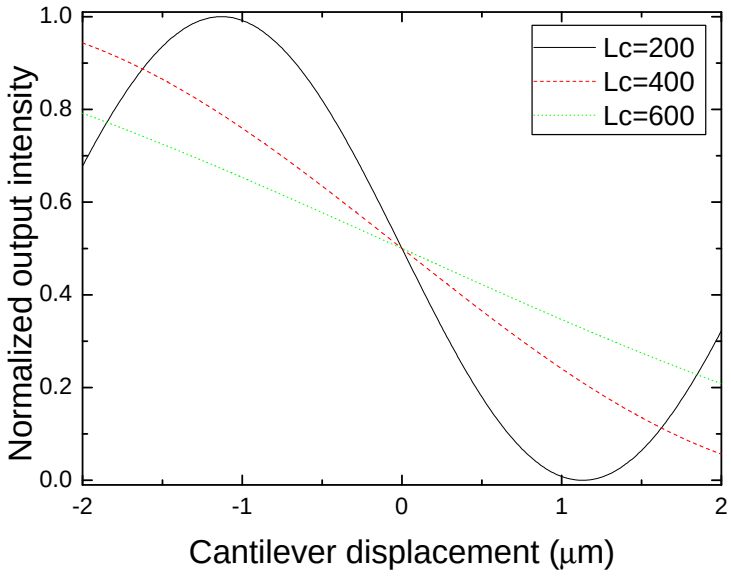

Figure 3. 4: Output intensity of Mach-Zehnder interferometer as a function of the cantilever displacement for three different cantilever lengths. The interferometer is unbalanced by changing the path length of the two arm in order to achieve steepest slope at $z = 0$

where L_{MZI} is the length of the MZI and C_T is the transverse stress optic coefficient. Using σ_{max} we get phase difference between the two arms as,

$$\Phi = \frac{2\pi n_{eff}}{\lambda}\Delta L + \frac{4\pi C_T}{\lambda}\frac{3Et}{2L_{can}^3} z \int_0^{L_{MZI}} (L_{can} - x)dL \qquad (3.\ 8)$$

ΔL is the path elongation and it was calculated using FEM for a $GaAs$ cantilever with length of 200 μm and thickness of 5 μm, $\Delta L = 0.019\ z$ where z is the displacement of the cantilever. ΔL is proportional with thickness and inversely proportional with length of the cantilever. From Eq. 3. 8 it is seen that the phase difference is a linear function of the displacement of the tip (z). As the cantilever displaces, the output intensity of the interferometer changes. Fig. 3. 4 shows the output intensity as a function of the cantilever displacement for different cantilever lengths. It is seen that, output intensity is linear about $z = 0$. For non-contact atomic force microscopes cantilever vibrates about 100$\mathring{A}$ and in

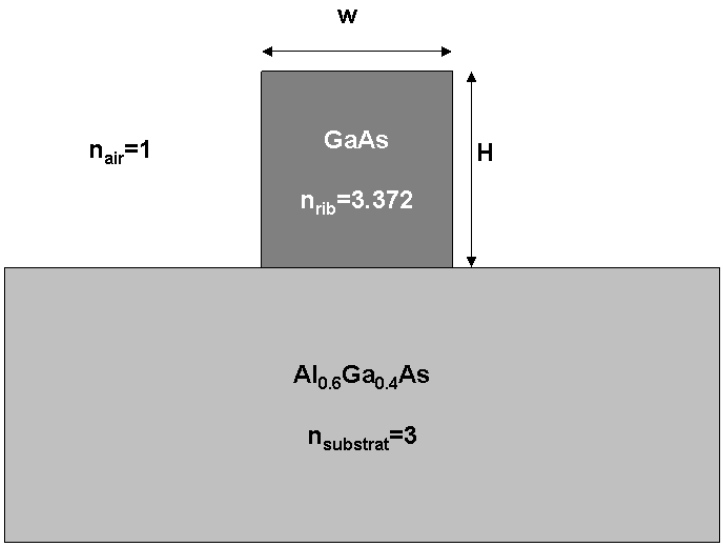

Figure 3. 5: Waveguide structure for Mach-Zehnder interferometer $w = 1\mu m$ and $H = 0.75\mu m$

order to get maximum sensitivity, the phase shift can be biased by changing the length of the two arms. For maximum sensitivity $L_1 - L_2 = \frac{\lambda}{8n_{eff}}$ is chosen.

3.3 Waveguide Design

Waveguide design is the central part of the interferometer. The interferometer can be divided into two parts; Y-junction and the curved waveguide on the cantilever. The waveguide must be single mode. Multimode waveguide decreases the visibility of the interferometer which also decreases the sensitivity. High index contrast must be chosen in order to decrease bending losses.

Fig. 3. 5 shows the single mode waveguide structure for $w = 1\ \mu m$ and $H = 0.75\ \mu m$. Stress reaches its maximum value at the surface and to get homogenous stress H must be small compared to the cantilever thickness. Bending losses are another important design consideration. Fundamental limitation is the bending of the waveguide on the cantilever with radius of less than 25 μm. Above waveguide

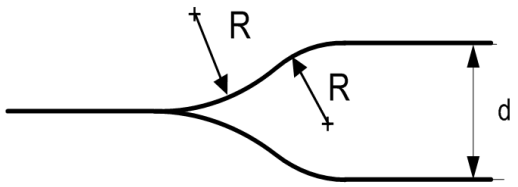

Figure 3. 6: Y junction

structure provides bending loss of less than 10 dB for $R > 9\mu m$ radius. Another important design consideration is the Y-junction. We choose a standard s-bend Y junction, the angle of the junction must be less than 1 degree in order to support adiabatic transition of the mode. For this structure, radiation loss is negligible due to the high index contrast. Fig. 3. 6 shows a typical Y junction where the radius of curvature is about 50000 μm and distance d is 50 μm. The input straight waveguide must be long enough to eliminate the radiative modes before the Y-junction.

3.4 Sensitivity Analysis

Sensitivity of the microscope is one of the parameters that defines the performance of the microscope. The resolution of a scanning microscope is directly related to the sensitivity and the noise of the system. Sensitivity is defined as the normalized output intensity variation per unit displacement of the cantilever and it can be written as

$$S_d = \frac{\Delta I}{I_0 \Delta z} \tag{3. 9}$$

here ΔI is the output intensity variation and Δz is the displacement of the cantilever. This sensitivity is called displacement sensitivity and we can also

$L_{can}(\mu m)$	200	500	500	1000
$L_{MZI}(\mu m)$	150	150	300	700
$S_d(\mathring{A}^{-1})$	6.9 10^{-5}	2.0 10^{-5}	2.6 10^{-5}	1.4 10^{-5}

Table 3.1: Calculated displacement sensitivities.

define force sensitivity as the output intensity variation per unit force applied on the cantilever such as,

$$S_f = \frac{\Delta I}{I_0 \Delta F} \tag{3. 10}$$

Sensitivity can be calculated by taking the derivative of the output intensity as a function of the cantilever displacement. The important thing that has to be considered is that, the microscope must work at the most sensitive region where the slope is maximum. It should also mentioned that if we bias the phase difference by adjusting the path lengths, linear output can be achieved over a longer range ($\sim 1\ \mu m$) which means constant sensitivity. The calculated displacement sensitivities are summarized in Table 3.1.

3.5 Experimental Setup

Experimental setup for this method is simple. It requires a light source and a photodetector. Another advantage of the MZI is that it is a broad band interferometer. The output intensity does not change due to the wavelength variation of the light source. Intensity variation of light source is the main noise source of the system. To eliminate the intensity variation a directional coupler can be used with a differential amplifier.

Chapter 4

Bragg Gratings

In this chapter a Bragg grating (BG) will be introduced as a displacement sensor for scanning force microscopes. BG is placed on the cantilever near the supporting point and as the cantilever displaces the generated stress changes the reflection spectrum of the BG. Using a narrow band light source it is possible to detect the displacement directly from the intensity modulation. In Section 4.1 basic operational principles will be discussed. In Section 4.2 cantilever design consideration will be given. In Section 4.3 design of Bragg Grating will be discussed.

4.1 Operation Principles

Bragg gratings (BG) are extensively used as a wavelength selective elements in optical devices. A BG is formed by creating a periodic corrugation or refractive index modulation in optical waveguides or fibers. BGs are useful because of their frequency dependent reflection spectrum. They are, in general, characterized by a central wavelength and the bandwidth of the reflection band. These structures can be thought of as one dimensional diffraction gratings which diffract light from a forward travelling mode into a backward travelling mode. From the well known Bragg condition, the central wavelength of the grating can be written as

$$\lambda_B = m2n_{eff}\Lambda \tag{4. 1}$$

where n_{eff} is the effective index of the structure and Λ is the period of the grating and m is an integer number. The bandwidth of BG, $\Delta\nu$, is proportional to the effective index modulation Δn_{eff} and is approximately given by

$$\frac{\Delta\nu}{\nu} = \frac{\Delta n}{n_{eff}} \tag{4. 2}$$

The effect of the grating on the propagation of light in the waveguide can be modelled using coupled-mode theory (CMT). CMT [26] predicts that the peak reflectivity of a BG is given by

$$R_{max} = tanh^2(\kappa L) \tag{4. 3}$$

where L is the grating length and κ is the grating strength (coupling coefficient). Waveguide Bragg gratings can be formed by physically corrugating the waveguide surfaces as is done in DFB lasers. Reflection spectrum of BG depends on the effective index of the waveguide, any variations of the refractive index result in change of reflection spectrum. Therefore, Bragg gratings have been applied to sense a number of physical values including strain [32], temperature [33] and magnetic fields [34]. These applications are based on the same principle, i.e: measurement of Bragg wavelength shift caused by external effects. In all these methods, a broad band optical source such as a LED, or a superfluorescent device

is used as the light source. To measure the shift in wavelength, external spectrum analyzers are employed. Recently many signal-processing methods are developed to directly measure the intensity modulation of the reflected light [35]. In one method, a light source with a very narrow spectral width such as DFB laser, is used in conjunction with a BG. Typically a BG has much larger spectral width ($0.5\ nm$) than a DFB laser ($\sim 1\ pm$). If the laser wavelength coincides within the reflection spectrum of the BG, the reflected light associated with the laser can be detected at the output. The output intensity at the detector is proportional to the overlap integral of the function $f(\lambda - \lambda_L)$ and $g(\lambda - \lambda_g)$ representing the spectral characteristics of the laser and BG, respectively [35]. Assuming these functions as Gaussians, we can write,

$$f(\lambda - \lambda_L) = P_0 \frac{2}{\Delta\lambda_L}\sqrt{\frac{ln2}{\pi}} exp[-4ln2(\frac{\lambda - \lambda_L}{\Delta\lambda_L})^2] \quad (4.\ 4)$$

$$g(\lambda - \lambda_g) = Rexp[-4ln2(\frac{\lambda - \lambda_g}{\Delta\lambda_g})^2] \quad (4.\ 5)$$

where $\Delta\lambda_L$ and $\Delta\lambda_g$ are the spectral widths and λ_L and λ_g are the central wavelengths of laser and grating, respectively and P_0 is the total power of the laser and R is the reflectivity of the grating. The overlap integral can be written as

$$I_{out} = \int_0^\infty f(\lambda - \lambda_L) g(\lambda - \lambda_g) d\lambda \quad (4.\ 6)$$

Since spectral width of BG, $\Delta\lambda_g$, is much larger than that of the laser, $\Delta\lambda_L$, I_{out} is

$$I_{out} \simeq P_0 g(\lambda_L - \lambda_g) \quad (4.\ 7)$$

$$I_{out} = P_0 Rexp[-4ln2(\frac{\Delta\lambda_c}{\Delta\lambda_g})^2] \quad (4.\ 8)$$

where

$$\Delta\lambda_c = \lambda_L - \lambda g \quad (4.\ 9)$$

Defining Bragg wavelength as;

$$\lambda_g = 2n_{ef}\Lambda \quad (4.\ 10)$$

we can write,

$$I_{out} = P_0 Rexp[-4ln2(\frac{\lambda_L - 2n_{ef}\Lambda}{\Delta\lambda_g})^2] \quad (4.\ 11)$$

From Eq. 4. 11 it is clearly seen that output intensity depends on the effective index of the grating. Any changes in effective index of the grating due to external effects, modulates the output intensity. From this modulation, it is possible to determine the external physical quantity. The most sensitive operation can be achieved by tuning the laser wavelength such that $\Delta\lambda_c = \Delta\lambda_g/2$ where the slope of reflection onset is maximum. Among the advantages of this method are that, it does not require any spectrum analyzer or a filter, it is optical and integrated. It should also be mentioned that I_{out} strongly depends on the reflection spectrum. Narrow band-width provides higher intensity variation with small index change.

4.2 Cantilever Design

In any cantilever design , the measurement of the displacement of the cantilever with high sensitivity is the essential task. The design of the cantilever and the type of the integrated sensor plays a fundamental role to increase the sensitivity. Perviously, much work have been done to enhance the sensitivity of AFM [36]. Bending of the cantilever generates stress which is the necessary physical quantity used to characterize the displacement of the cantilever. Figure 4. 1 shows the

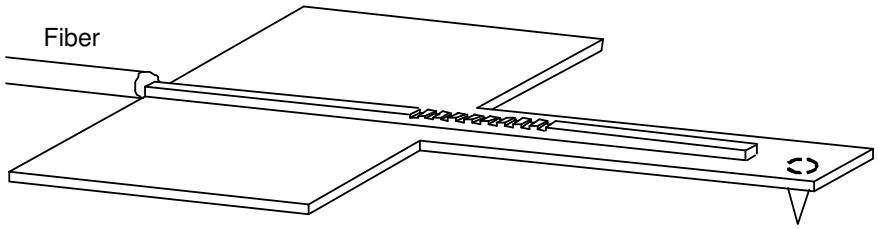

Figure 4. 1: Schematics of cantilever integrated with a Bragg grating.

schematics of the cantilever integrated with a Bragg grating. Bragg grating is loaded on the supporting point of the cantilever. Photo-elastic effect is used for

the sensing mechanism; stress generated on the cantilever changes the refractive index of the waveguide where the BG is loaded. Furthermore, sensing the generated stress using integrated optical devices requires materials suitable for such devices with large stress optic coefficients. A good candidate is GaAs. Applying mechanical stress to GaAs results in variation of local index due to photo-elastic effect. Since the displacement of the tip causes a mechanical stress along the cantilever, maximizing the stress on the sensing element will maximize the performance. Therefore the sensing element is placed at the supporting point where the stress reaches its maximum value of

$$\sigma_{max} = \frac{3Et}{2l^2} z \tag{4. 12}$$

where, E is the Young's Modulus, t is the thickness, l is the length and z is the displacement of the cantilever. The design of the grating, waveguide and cantilever is related to the stress distribution on the cantilever. For FEM simulations, Young's Modulus of 0.86 $\times$ 10^{11} N/m^2, and Poisson's ratio of 0.31 were used. Static analysis was performed using ANSYS software. The mesh was increased in the waveguide region where the grating sensor is placed. Maximum stress occurs at the supporting point of the cantilever and decreases linearly along the cantilever. The analysis performed here uses the stress at the surface of the cantilever. Stress reaches its maximum value on the surface and decreases along the thickness of the cantilever. The waveguide height is much smaller than the cantilever thickness therefore the variation of the stress along the waveguide height is neglected and an average value is used. We will use these results in the design of the sensor and calculation of the sensitivity. Through the photo-elastic effect index change can be written as [26]

$$n_{eff} = n_0 + \sum_i C_i \sigma_i \tag{4. 13}$$

where C_i is the stress optic constant of the waveguide and σ_i is the local stress. For GaAs, longitudinal stress optic coefficient C_l=1.0 $\times$ 10^{-11} Pa^{-1} and transverse stress optic coefficient C_t = 1.7 $\times$ 10^{-11} Pa^{-1}. Longitudinal stress on the cantilever surface is much larger than the transverse stress, therefore we can

neglect the transverse stress and,

$$\Delta n \simeq C_l \sigma_l \simeq \frac{3C_l E t}{2l^2} z \tag{4. 14}$$

and the effective index becomes,

$$n_{eff} = n_0 + \frac{3C_l E t}{2l^2} z \tag{4. 15}$$

Putting this equation into Eq.**??**, the output intensity as function of cantilever displacement is obtained as,

$$I_{out} = P_0 R exp[-4ln2(\frac{\lambda_L - 2\Lambda(n_0 + \frac{3C_l E t}{2l^2} z)}{\Delta\lambda_g})^2] \tag{4. 16}$$

From Hooke's law, force on the tip can be expressed as

$$F = kz = \frac{wEt^3}{4l^3} z \tag{4. 17}$$

where k denotes the spring constant of the cantilever. Using Eq. 4. 16, Eq. 4. 17 can also be written as a function of force applied on the tip

$$I_{out} = P_0 R exp[-4ln2(\frac{\lambda_L - 2\Lambda(n_0 + \frac{6C_l l}{wt^2} F)}{\Delta\lambda_g})^2] \tag{4. 18}$$

Eq. **??** and Eq. 4. 18 show that by measuring the output intensity, it is possible to calculate the displacement of the cantilever and the force applied on it. It can be seen that local index variation and therefore the output intensity is strongly dependent on the geometry of the cantilever and the spectrum of the Bragg grating.

4.3 Bragg Grating Design

Waveguide Bragg grating is designed to be fabricated on a single mode $GaAs/GaAlAs$ waveguide. The operational parameters for the BG are the period and the etch depth of the grating. The central wavelength can be controlled by tuning the period and the coupling coefficient can be controlled by tuning the

etch depth. By choosing the Al concentration at %20 it is possible to have an index difference of 0.12 and choosing the core height as 1 μm and ridge width as 2 μm a single mode waveguide can be obtained. The mode spectrum of the such a waveguide was calculated using a Beam Propagation Method (BPM) simulation to confirm the single mode behavior. The analysis of the grating has been carried out by calculating the coupling coefficient κ. Using CMT, κ can be written as [38]

$$\kappa = \frac{{k_0}^2}{2\beta N^2} \int_{corrugate} \Delta[n^2(x,z)] E^2 dx \qquad (4.\ 19)$$

where $k_0 = \frac{2\pi}{\lambda_0}$ and β is the propagation constant, E^2 is the electric field profile and N^2 is the normalization constant given as

$$N^2 = \int_{-\infty}^{\infty} E^2 dx \qquad (4.\ 20)$$

Fig. 4. 2 shows the calculated coupling coefficient for this waveguide as a function of grating height (tooth height) for three different duty cycles. For a first order diffraction grating with grating height of $h(= 0.1\ \mu m)$ the coupling coefficient is seen to be $\kappa = 0.01\ \mu m^{-1}$ for a duty cycle of 0.35 . Small grating depth is chosen to minimize optical loss. In order to make the reflectivity R larger than 0.9 it must be such that $\kappa L \geq 2.18$, therefore minimum grating length must be $L \geq 200\ \mu m$ which is suitable for cantilever design. It should be noted that there is a tradeoff between L and κ due to the fact that to get higher reflectivity κ must be increased which causes the broadening of the spectral response leading to a decrease in sensitivity. An other important parameter that determines the the coupling coefficient is the duty cycle. Duty cycle of a grating is defined as the ratio of grating tooth to grating period. In Fig. 4. 3, we plot the coupling coefficient as a function of duty cycle for various grating depths. One interesting result which is observed from Fig. 4. 3 is that the strongest coupling occurs when the duty cycle is smaller than 0.5. In our design, a duty cycle of 0.35 was chosen to obtain the largest coupling coefficient. Fig.4. 4 shows the calculated reflection spectrum of the BG about the central wavelength of 1.55 μm. This spectrum is

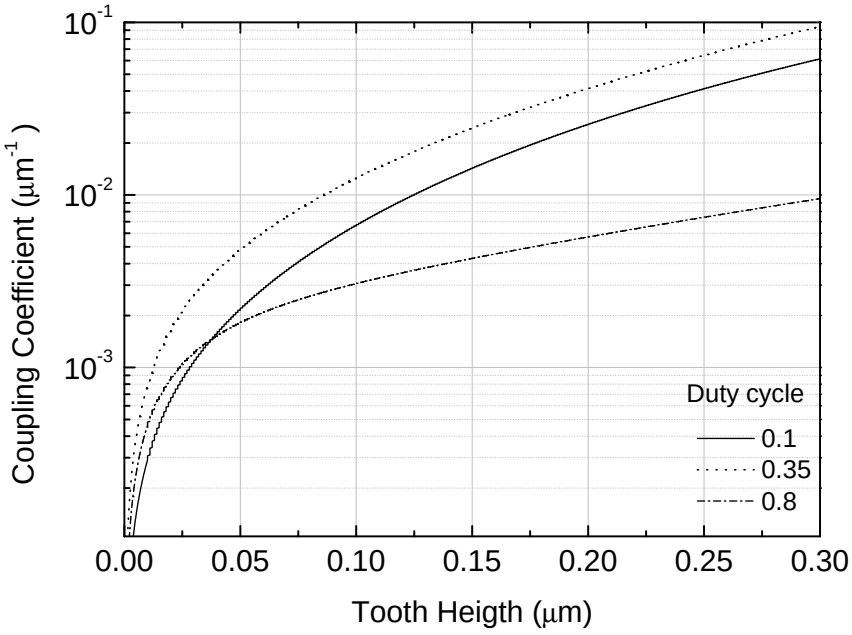

Figure 4. 2: Calculated coupling coefficient as a function of grating height for three different duty cycles.

calculated using TMM simulation. In the simulation, we use the effective index change (δn) calculated from the coupling coefficient such as

$$\delta n = \frac{\kappa\lambda}{\pi} \tag{4. 21}$$

which shows good agrement with that obtained from CMT. In order to get high sensitivity a Bragg grating with a high reflectivity and narrow spectral width is used. From the above calculation, a BG with 0.9 reflectivity and 3 nm reflection band width was obtained. In the next section, further improvement of these parameters is presented.

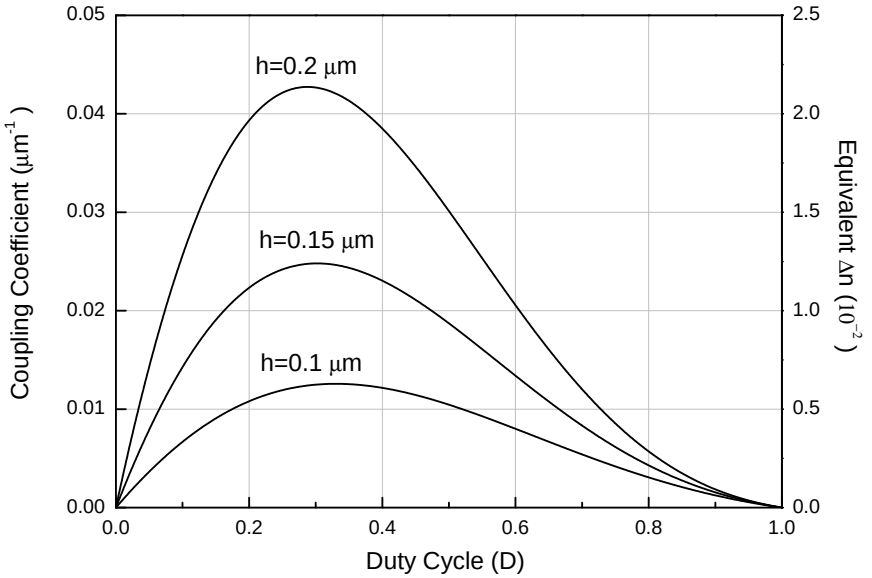

Figure 4. 3: Calculated coupling coefficient as a function of duty cycle.

4.4 Quarter-wave Shifted Bragg Grating

The sensitivity of a BG sensor strongly depends on the reflectivity spectrum and hence the bandwidth of the sensor. A further improvement of the design can be made using narrow band highly reflective filters. One way to implement a narrow band filter is to use a quarter-wave shifted Bragg Grating (QWBG). In 1977, Haus [39] showed that insertion of a quarter wave shift at the center of Bragg grating provides a single narrow band pass filter in the stop band of the BG. The transmission spectrum of the BG with a quarter wave phase shift region in the middle of the BG is shown in Fig. 4. 5. Very narrow transmission can be achieved. Because of their higher reflectivity and narrower band width, QWBGs have found widespread application in field of optical communications especially in dense wavelength-division multiplexing (DWDM) and DFB laser technology. In this section, we discuss the application of these filters for AFM as a displacement sensor. We can model a QWBG as Fabry-Perot resonator

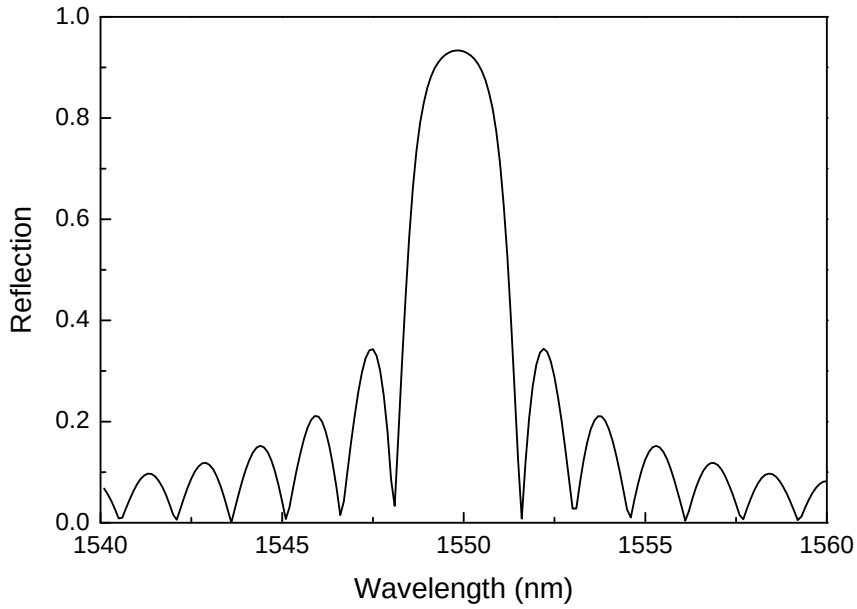

Figure 4. 4: Calculated reflection spectrum for 250 μm long Bragg grating with 0.210 μm period and 0.1 μm grating height.

with the gratings serving as wavelength selective mirrors of identical reflection spectrum separated by a quarter wave shifted region. When the length , L, of the quarter phase shift region satisfies the phase matching condition ($\mathrm{L} = (n+1)\frac{\lambda}{4}$), a strong and narrow transmission band appears in the middle of the stop band region. The transmission band width depends quantitatively on the coupling strength and length of the gratings mirror and waveguide loss. Using the same analysis as in the previous section, it is possible to have a bandwidth of 0.5 $\mathring{A}$ and transmission of $T \geq 0.9$ which makes the this sensor more sensitive than the standard BG by two orders of magnitude. The peak position is very sensitive to the refractive index of the phase shift region. Very small index changes results in the change of the peak position. This can be used to sense the cantilever deflection. A narrow band laser is tuned to the transmission wavelength and by monitoring the intensity variation due to the shift of the transmission wavelength,

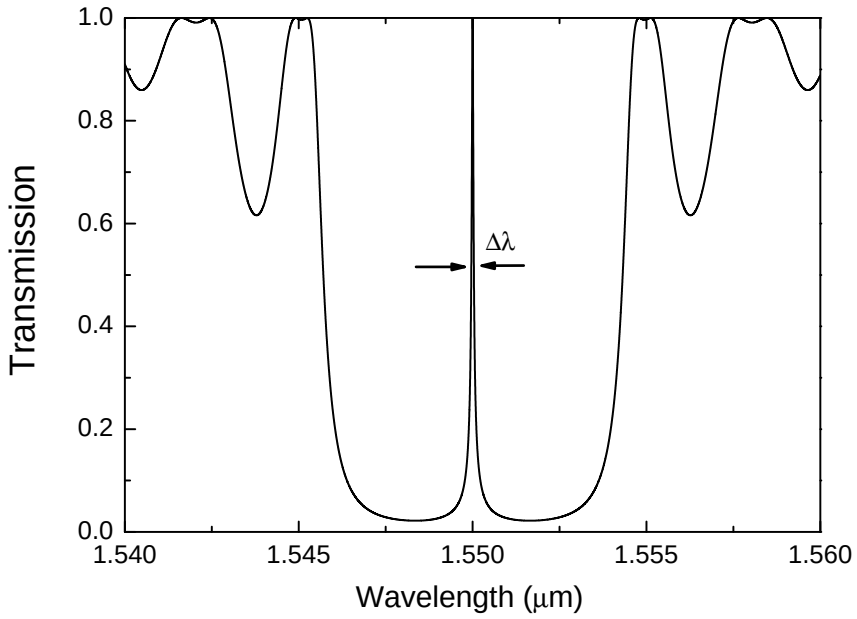

Figure 4. 5: Calculated transmission spectrum for quarter-wave shifted Bragg grating. Very narrow transmission band can be achieved ($\Delta\lambda = 0.5\mathring{A}$)

it is possible to detect the cantilever displacement. Fig. 4. 6 shows the output intensity variation as a function of the index change of the grating for different cavity lengths. Longer phase shifted regions provide more sensitivity for index change. Fig. 4. 7 depicts the normalized output intensity variation as a function of the cantilever displacement. It is clearly seen from the graph that for small displacement, the output intensity variation increases much more rapidly and is exponentially depended on the cantilever deflection.

4.5 Experimental Setup

The design of experimental setup is very similar to fiber optic interferometer setup. A narrow band DFB laser with fiber output is used as the light source. The output of laser is split into two with a directional coupler one of which

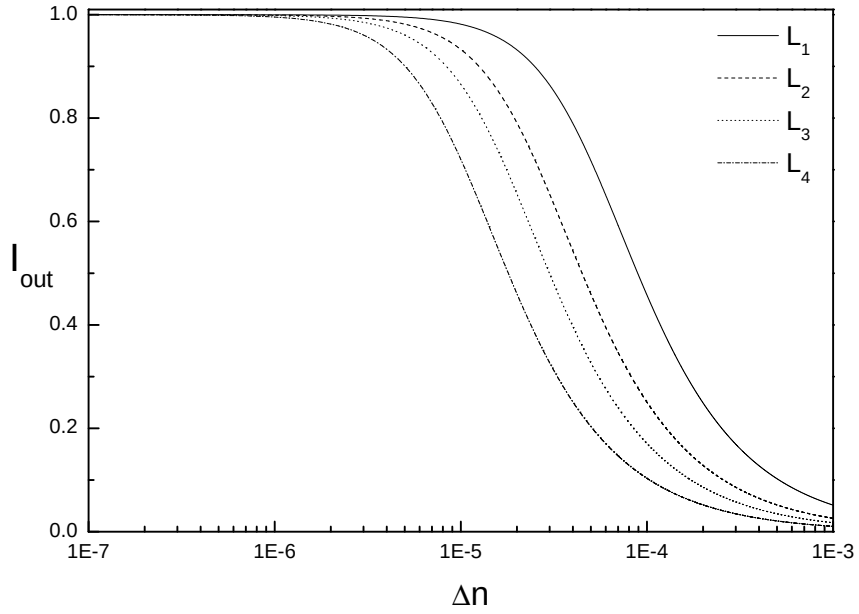

Figure 4. 6: The normalized output intensity variation as a function of the index change of the grating for different cavity lengths. Where L_1, L_2, L_3, L_4 are $101\frac{\lambda}{4}$, $201\frac{\lambda}{4}$, $301\frac{\lambda}{4}$, $501\frac{\lambda}{4}$, respectively.

is used as reference to eliminate the intensity fluctuation of the laser. The other output is butt-coupled to the waveguide on the cantilever and reflected light from BG is detected with a photodetector via the same directional coupler. Fluctuations of the laser wavelength causes intensity variations at the output. Lock-in amplification is necessary to eliminate the random intensity variation.

4.6 Sensitivity

The enhancement of force and displacement measurement sensitivity is of great interest since smaller deflections can be measured with greater accuracy. It should be mentioned that previous integrated sensors provide less sensitivity than the external ones (i.e. Fabry-Perot interferometer). With this new design,

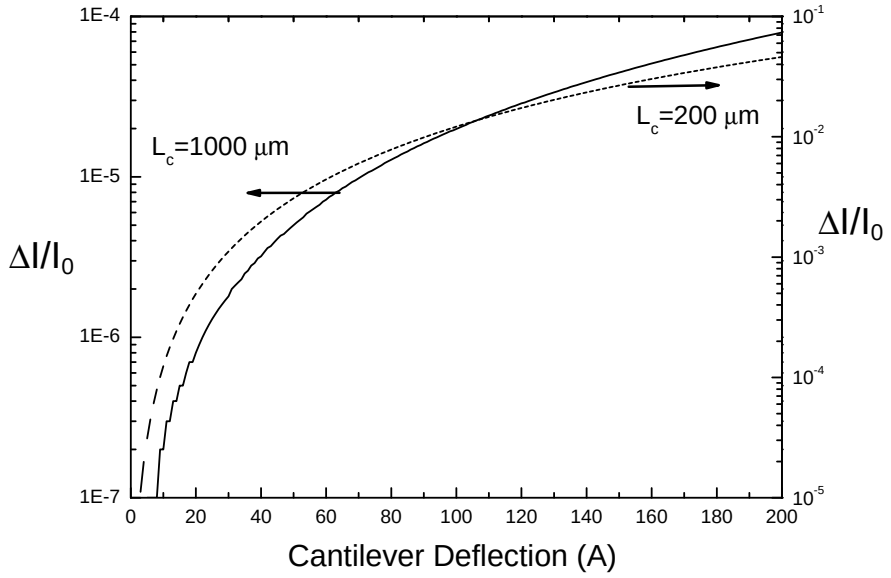

Figure 4. 7: The normalized output intensity variation as a function of the cantilever displacement for 200 and 1000 μm long cantilevers thickness of 5 μm and width of 50 μm.

the sensitivity can be enhanced by two orders of magnitude. Sensitivity can be defined as the variation of current on photodetector (PD) per unit displacement of cantilever. Current on PD is proportional to the intensity of the light falling on it, so that

$$\frac{\Delta i}{i} = \frac{\Delta I_{out}}{I_0} \tag{4. 22}$$

from Eq.12

$$\frac{\Delta I_{out}}{I_0} = R4ln2(\frac{\Delta\lambda_c}{\Delta\lambda^2})exp[-4ln2(\frac{\lambda-\lambda_g}{\Delta\lambda})^2]\frac{d\lambda}{dz}\Delta z \tag{4. 23}$$

We can write λ_g in terms of displacement or force on the cantilever

$$\lambda_g = 2\Lambda(n_0 + \frac{3C_lEt}{2l^2}z) = 2\Lambda(n_0 + \frac{6C_ll}{wt^2}F) \tag{4. 24}$$

leading to

$$\frac{d\lambda_g}{dz} = \frac{3\Lambda C_lEt}{l^2} \tag{4. 25}$$

or

$$\frac{d\lambda_g}{dF} = \frac{12\Lambda C_l l}{wt^2} \tag{4. 26}$$

As a result, we can define displacement sensitivity as;

$$S_d = \frac{\Delta I_{out}}{I_0 \Delta z} = R\frac{12ln2\Lambda C_l E t}{l^2}(\frac{\Delta\lambda_c}{\Delta\lambda^2})exp[-4ln2(\frac{\lambda_c L - \lambda_g}{\Delta\lambda})^2] \tag{4. 27}$$

and force sensitivity as,

$$S_f = \frac{\Delta I_{out}}{I_0 \Delta F} = R\frac{48ln2\Lambda C_l l}{wt^2}(\frac{\Delta\lambda_c}{\Delta\lambda^2})exp[-4ln2(\frac{\lambda_L - \lambda_g}{\Delta\lambda})^2] \tag{4. 28}$$

Photo elastic deflection sensitivity is given in Eq. 4. 27. This defines the changes in the output intensity per unit displacement of the cantilever. From Eq. 4. 27 it is understood that displacement sensitivity depends on Young's Modulus and stress optic coefficient. In order to achieve high sensitivity, we should choose our cantilever material such that it has high Young's modulus and stress optic coefficient. GaAs is a very good material for displacement measurements. Force sensitivity can be defined as change in the output intensity per unit force applied on the cantilever. From Eq. 4. 28, we can conclude that force sensitivity does not depend on the Young's modulus. This allows us to fabricate cantilevers from materials which have low Young's modulus but has large stress optic constant such as some polymers. We also conclude from Eq. 4. 27 and Eq. 4. 28 that a short and thick cantilever is sensitive to displacement measurements whereas long and thin cantilevers are more sensitive to force detection. Fig. 4. 7 shows normalized intensity change as a function of the cantilever displacement. Additional improvement of sensitivity can be achieved by modifying the geometry of the cantilever. Maximizing the stress in the grating region will maximize the sensitivity. Bashir *et. al* [36] have introduced stress concentration regions on the cantilever and this method can also be applied to our design to increase sensitivity.

Chapter 5

Micro-Ring Resonators

5.1 Physical Considerations

In this chapter we use a micro-ring resonator integrated on a cantilever as a displacement sensor. This sensor is based on the photo-elastic effect. The atomic forces make the cantilever deflect from equilibrium and this deflection produces stress on the cantilever surface. Index change on the ring due to the stress cause a shift in the resonant wavelength. Fig. 5. 1 shows the transmission spectrum of optical waveguide coupled ring resonator and the modulation concept. Stress on the ring causes shift in the resonance wavelength. The stress reaches its maximum value at the supporting point of the cantilever and it decreases linearly along the cantilever. Maximum stress as a function of displacement, z can be written as;

$$\sigma_{max} = \frac{3Et}{2l^2} z \tag{5. 1}$$

where E is the Young's modulus of the cantilever material, t is the thickness, and l is the length of the cantilever. Due to the photo-elastic effect, effective index changes due to the stress and through the equation,

$$n_{eff} = n_0 + \sum_i C_i \sigma_i \tag{5. 2}$$

where, C_i is the stress optic constant of waveguide and σ_i is the local stress. Longitudinal stress is much larger than the transverse stress, which can be

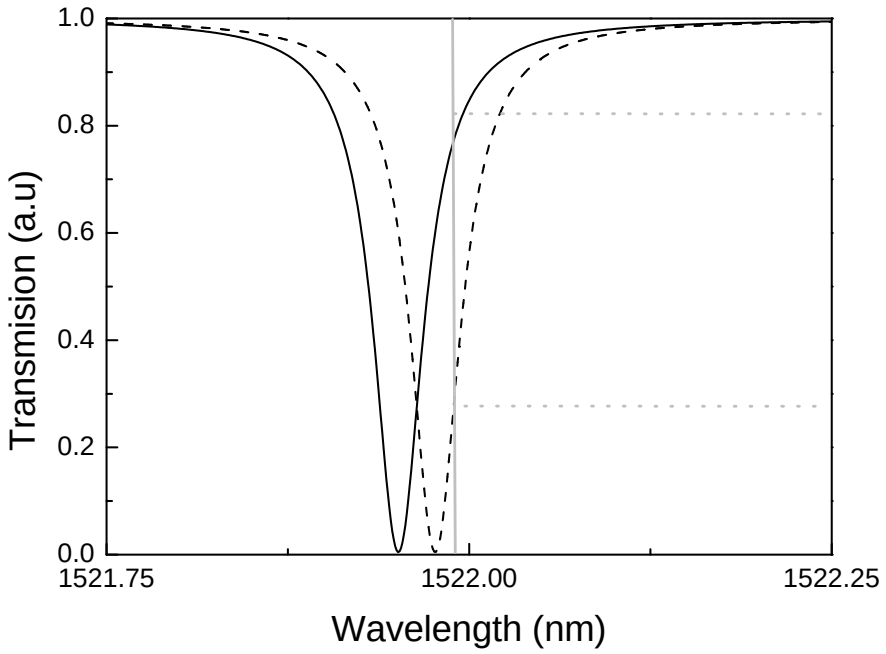

Figure 5. 1: Sensor concept based on a ring resonator. The optical power modulation takes place as position of resonance dip shifts. Inset shows the variation of the output intensity.

neglected, so that

$$\Delta n_{max} \simeq C_l \sigma_l \simeq \frac{3C_l E t}{2l^2} z \tag{5. 3}$$

Refractive index change can also be written as function of the force applied on the tip. From Hooke's law, force on the rectangular cantilever can be expressed as

$$F = kz = \frac{wEt^3}{4l^3} z \tag{5. 4}$$

where k denotes the spring constant of the cantilever, then refractive index change can be written as,

$$\Delta n_{max} \simeq \frac{6C_l l}{wt^2} F \tag{5. 5}$$

From Eq. 5. 3 and Eq. 5. 5, the refractive index change depends on the geometry of cantilever and photo-elastic constant of the material. Total accumulated phase

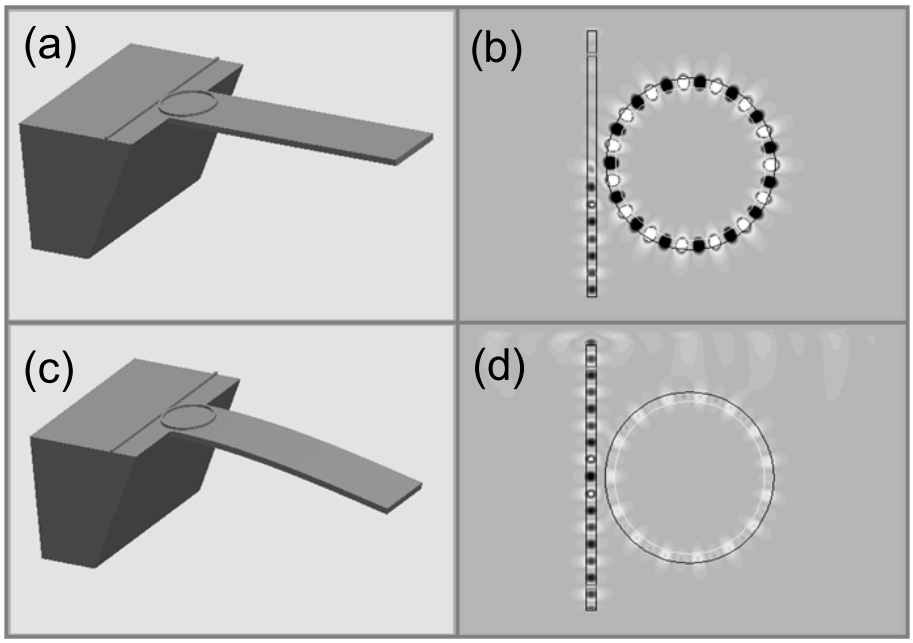

Figure 5. 2: A schematic illustration of the operational principle for the integrated micro-ring resonator displacement sensor, (a and c) shows the cantilever for unbent and bent condition, (b and d) shows the field distribution on the ring resonator on the cantilever.

on the ring can be written as,

$$\Delta\Phi = \frac{2\pi}{\lambda}\int_{ring}\Delta n\ dl \simeq \frac{2\pi C_l}{\lambda}\int_{ring}\sigma_l\ dl \qquad (5.\ 6)$$

where λ is the wavelength. In order to achieve large phase shifts, total length of the ring must be kept large and the cantilever material with a large elasto-optic coefficient must be chosen. Figure 5. 2 shows the schematics of micro-ring resonator displacement sensor. Figure 5. 2 a and c shows the unbent and bent cantilevers, b and d show the field distribution of the micro-ring resonator. As the cantilever displaces the transmission of the ring resonator changes.

5.2 Analysis and Design of Micro-Ring Resonators

Micro-ring resonators are of great interest due to their compactness, the fact that they do not need facets or gratings for optical feedback, stability with respect to back reflections and high wavelength selectivity, which are key features for various applications. They mainly find applications in wavelength division multiplexing (WDM) [40] and wavelength add-drop systems [41] for optical communications. Ring resonators are not only good candidates for WDM and add/drop filters but also well suited for routing [42] , switching and modulation applications [43] .

5.2.1 Ring Resonator Analysis: Single Bus System

A ring resonator system is composed of one or two bus waveguides and a ring placed very close to them as shown in Fig. 5. 3. There are several figures of merit for a ring resonator. These are the modulation depth which shows the depth of the on/off ratio (in dB), free spectral range (FSR) which is the wavelength spacing between adjacent resonances, full width at half maximum (FWHM) of each resonance which shows how narrow the peak is at the resonance wavelength. The Q factor gives the ratio of resonance wavelength to FWHM of the resonance. Depending on the application, large or small values for FSR may be desirable but small FWHMs, large modulation depths and large Q factors always preferred.

Consider the single bus coupled ring structure in Fig. 5. 3a. The general matrix for outgoing waves in terms of incoming waves in the coupling region of the system [44] is

$$\begin{pmatrix} b1 \\ b2 \\ b3 \\ b4 \end{pmatrix} = \begin{pmatrix} 0 & (1-k^2)^{1/2} & 0 & ik \\ (1-k^2)^{1/2} & 0 & ik & 0 \\ 0 & ik & 0 & (1-k^2)^{1/2} \\ ik & 0 & (1-k^2)^{1/2} & 0 \end{pmatrix} \begin{pmatrix} a1 \\ a2 \\ a3 \\ a4 \end{pmatrix} \quad (5.\ 7)$$

Here, $|k|^2$ is the fraction of power coupled between waveguide and ring, so that $1-|k|^2$ is the transmitted portion of the power that is not coupled to the ring.

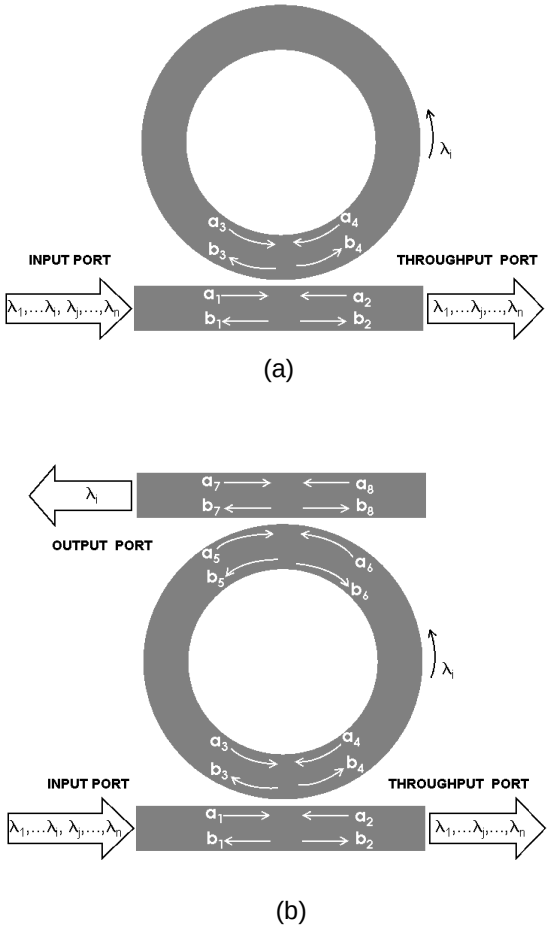

(a)

(b)

Figure 5. 3: Schematic representation of single bus (a) and double bus (b) ring resonator and the relevant propagating field amplitudes.

In the case of no back reflections and a_1 being the input wave,

$$a_2 = a_4 = b_1 = b_3 = 0 \tag{5. 8}$$

Then, solving the matrix for the remaining terms leads to transmitted amplitudes as

$$b_2 = (1 - k^2)^{1/2}\ a_1 + ika_3 \tag{5. 9}$$

and

$$b_4 = (1 - k^2)^{1/2}\ a_3 + ika_1 \tag{5. 10}$$

Matching the travelling waves in the ring gives,

$$a_3 = b_4 \exp\left(-(\alpha_T + i\phi)\right) \tag{5. 11}$$

and using it to eliminate a_3 in the above equations results in

$$b_2 = \frac{(1-k^2)^{1/2} \ - \exp\left(-(\alpha_T + i\phi)\right)}{1 - (1-k^2)^{1/2} \ \exp\left(-(\alpha_T + i\phi)\right)} \tag{5. 12}$$

where, α_T and ϕ are optical loss and phase accumulated per round trip in the ring, respectively. For a resonator of length L $(= 2\pi R)$, optical loss coefficient α and effective refractive index of n_e,

$$\alpha_T = \alpha L \tag{5. 13}$$

and

$$\phi(\lambda) = \frac{2\pi}{\lambda} n_e L \tag{5. 14}$$

where λ is the free space wavelength. The resonance takes place when $\phi = 2\pi m$, and m is an integer number. Then, the resonance field amplitudes become

$$b_2 = \frac{(1-k^2)^{1/2} \ - \exp\left(-\alpha_T\right)}{1 - (1-k^2)^{1/2} \exp\left(-\alpha_T\right)} a_1 \tag{5. 15}$$

and

$$b_4 = \frac{ik}{1 - (1-k^2)^{1/2} \exp\left(-\alpha_T\right)} \ a_1 \tag{5. 16}$$

An obvious result is that if

$$(1-k^2)^{1/2} = \exp\left(-\alpha_T\right) \tag{5. 17}$$

no power is reflected so that $b_2 = 0$. This is the so-called critical coupling condition and all the power is coupled to the ring. One has to take square of the field b_2 and b_4 to find the corresponding optical intensities in terms of the input optical power. Therefore, the transmitted power is

$$I_t = |b_2|^2 = |\frac{(1-k^2)^{1/2} \ - \exp\left(-(\alpha_T + i\phi)\right)}{1 - (1-k^2)^{1/2} \ \exp\left(-(\alpha_T + i\phi)\right)} \ a_1|^2 \tag{5. 18}$$

5.2.2 Ring Resonator Analysis: Double Bus System

The above treatment can be easily extended a ring structure coupled to two bus ring structure as shown in Fig. 5. 3b. When there is a second bus, there will be a second coupling region allowing for the out coupling of trapped light in the ring. The expression for reflected power is exactly the same as in the single bus system apart from a change in the loss term to account for the coupled power to the second bus. The new loss term is

$$\alpha_{eff} = -\ln\left(1-k_2^2\right)^{1/2} + \alpha_T \tag{5. 19}$$

So, the new transmitted intensity is

$$I_t = \left|\frac{(1-k^2)^{1/2} - \exp\left(-(\alpha_{eff}+i\phi)\right)}{1-(1-k^2)^{1/2}\ \exp\left(-(\alpha_{eff}+i\phi)\right)}\ a_1\right|^2 \tag{5. 20}$$

Here, $|k_1|^2$ is $|k|^2$ and $|k_2|^2$ is the fraction of power coupled between the second bus and the ring. In most cases $|k_1|^2 = |k_2|^2 = |k|^2$. Analyzing the resonances and imposing that no reflected power takes place, i.e. $I_t = 0$, gives the critical coupling condition for the double bus system as,

$$(1-k_1^2)^{1/2} = (1-k_2^2)^{1/2}\ \exp\left(-\alpha_T\right)\ or\ k_2 = \left(1-(1-k_1^2)\exp\left(2\alpha_T\right)\right)^{1/2} \tag{5. 21}$$

5.2.3 Waveguide Design

We design and analyze ring resonators on GaAs/AlGaAs platform. The waveguides designed are deeply etched to achieve strong confinement [45] , which is essential to minimize waveguide bending losses. The general waveguide structure is seen in Fig. 5. 4. The fraction of Al, x, and the geometry of the waveguide are chosen so that single mode propagation is assured. The basic limitation to the resonator and therefore to the waveguide design is the need to propagate light in a small radius of curvature of less than 25 μm with minimum loss, since the cantilever width is about 50 μm. In principle, we need to find the complex angular propagation constant, γ, for a bend of radius R, and using

$$n_{bend} = \frac{Re(\gamma)}{k_0 R} \tag{5. 22}$$

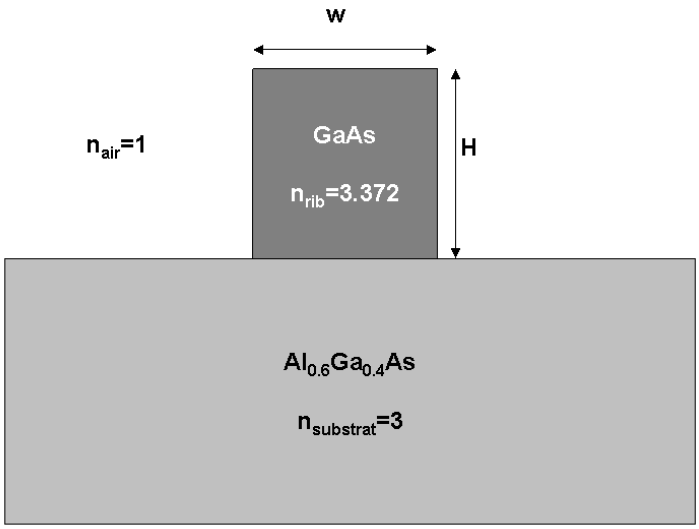

(a)

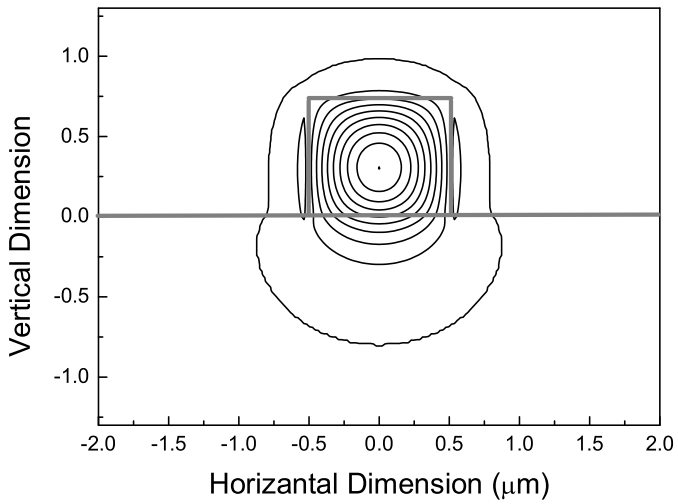

(b)

Figure 5. 4: Single mode waveguide structure (a), and its mode distribution (b).

to find effective refractive index of the bend [46] . The condition for guiding light in a bending waveguide is that n_{bend} should be larger than substrate refractive index, n_{sub} . Determining n_{bend} requires solving the wave equation in cylindrical coordinates or employing full numerical calculations of the propagation constant by beam propagation (BPM) or finite difference time domain (FDTD) methods both of which are tedious. As a first order approximation, we used an empirical equation [47] for the cut-off radius, R_{co}, in terms of waveguide width, w, refractive indices of straight waveguide, n_{str}, and substrate, n_{sub}, which is

$$R_{co} = \frac{w n_{rib}}{2(n_{str} - n_{sub})} \tag{5. 23}$$

A few trials with different Al mole fraction and waveguide width, w, and height, H led us to a single mode waveguide structure which can be fabricated using optical lithography. This structure has 0.6 as x, 1 and 0.75 μm as w and H respectively. n_{str} is 3.192 for TE polarization which is found by mode calculation using a commercial BPM program (see Fig.4b), $n_{rib} = n_{GaAs}$ is 3.372 and $n_{subst} = n_{AlGaAs}$ is 3.000. This structure gives an R_{co} of 9 μm. We choose it to be safe to use an R value of 20 μm for the ring.

5.2.4 Ring Resonator as Displacement Sensor

For the purpose of sensing displacement, we are mainly interested in modulation applications of ring resonators. It should be possible to obtain a large modulation in transmitted optical power by small variations of the refractive index. This kind of modulation is useful only if the resonance wavelength shift remains in the bandwidth of the resonator. Such shifts can only be achieved through a controllable change in optical path length of resonators, which is a function of resonator physical length and effective refractive index. Here, stress induced refractive index change is employed. When the ring resonator is designed to have a high-Q factor, the modulation is dramatic due to steep fall of the transmission dip. A ring resonator could have high Q-factors when designed to work at the critical coupling regime. As the operational principle of the ring resonator coupled waveguide sensor depends on the stress distribution along the cantilever,we

have calculated the 3D stress distribution using Finite Element Method (FEM) simulations, for which; Young's Modulus of 0.86 $\times 10^{11}$ N/m^2, and Poisson's ratio of 0.31 were used. Static analysis was performed using ANSYS software. The mesh was increased in the region where ring resonator was placed. The analysis performed here uses the stress at the surface. The local stress on the top surface decreases along the z direction and becomes negative on the opposite surface. Fig.

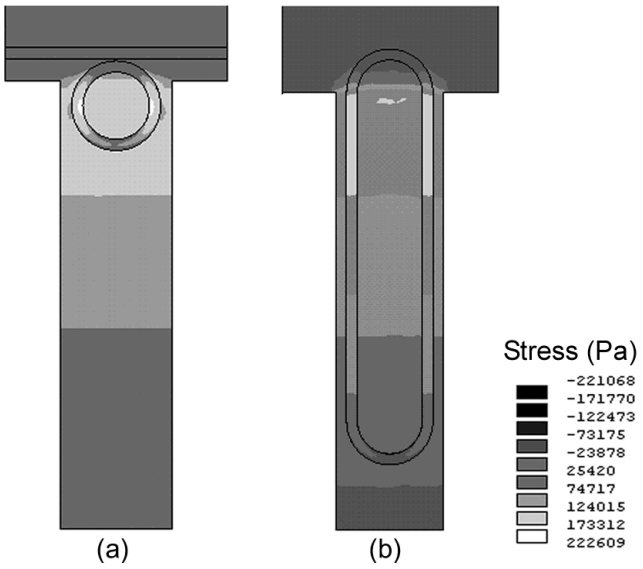

Figure 5. 5: Longitudinal stress distribution on the cantilevers with a ring (a) and a race-track (b) shape resonator. Long straight arms in the race-track resonators are useful for increasing the accumulated phase shift.

5. 5a shows the stress contours on the the ring resonator obtained from FEM simulation. Maximum stress occurs at the supporting point of the cantilever and decreases linearly along the cantilever. In Fig. 5. 6 we plot the stress distribution along the perimeter circumferences of the ring. From Fig. 5. 6, it is clearly observed that stress occurs on the two sides of the ring which are parallel with the major symmetry axis of the cantilever. Calculated total accumulated phase on the ring with radius of 20 μm is 1.6 10^{-3} rad for 100 $\mathring{A}$ cantilever deflection. In order to increase the accumulated phase shift, the parallel sides may be kept

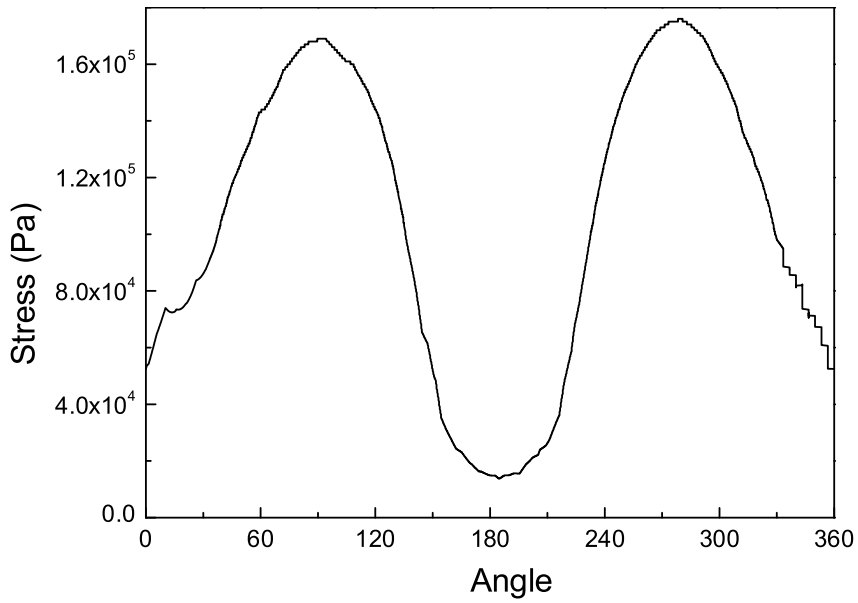

Figure 5. 6: Calculated stress distribution on the ring resonator as a function of the angle as measured from the major symmetry axis of the cantilever.

longer. The optimum design is a race-track shaped resonator, because of its two long parallel sides where stress is much larger than the curved sides. Fig. 5. 6b shows the stress contours on the race-track resonator. Phase shift can be approximated as;

$$\Delta\Phi \simeq \frac{3\pi C_l E t L_{rt}}{2\lambda l^2}\ z \tag{5. 24}$$

where L_{rt} is the length of the race-track resonator. From Eq. 5. 24, it is observed that the phase shift is linearly proportional to the cantilever deflection and it is related to the cantilever geometry and mechanical properties of the cantilever material. For higher sensitivity, total length of the ring and the elasto-optic coefficient of the material must be large. Phase shift can also be written as a function of force applied on the tip and,

$$\Delta\Phi \simeq \frac{6\pi C_l l L_{rt}}{\lambda w t^2}\ F \tag{5. 25}$$

where F is the applied force, w is the width of the cantilever. In order to increase the phase shift due to the applied force we have to keep the length long and the

thickness of the cantilever small which results in a trade of between force and displacement sensitivity. It is not possible to achieve high displacement sensitivity as well as high force sensitivity. We can conclude that short and thick cantilever is sensitive to displacement measurements whereas long and thin cantilevers is more sensitive for force detection. One interesting result which is seen from Eq. 5. 25 is that the phase shift does not depend on the Young's modulus of the cantilever.

5.3 Sensitivity Analysis

The sensitivity of displacement sensors is the essential property of the atomic force microscopies. The minimum detectable force and the displacement depend on the sensitivity of the sensor and the noise of the system. Integrated sensors have less sensitivity than external ones. There have been many studies to increase the sensitivity of the integrated sensor, but the best sensitivity achieved so far is $\sim 10^{-6}$ A^{-1} [49] , which is two orders of magnitude less than the sensitivity of the interferometric detection [11]. Force sensitivity can be defined as the variation of the current on the detector per unit force applied on the tip, with the same logic displacement sensitivity can be defined as the variation of the current on the detector per unit displacement of the cantilever. The current on the detector is proportional to the light falling on it,

$$i = \frac{\eta I_0}{h\nu} \tag{5. 26}$$

where η is the quantum efficiency of the photo detector, I_0 is the incident optical power, ν is the frequency of the light. Therefore

$$\frac{\Delta i}{i_0} = \frac{\Delta I}{I_0} \tag{5. 27}$$

The detected power, I_t depends on the transmission characteristics of the ring resonator coupled waveguide. Transmission of the single and double bus ring resonators are given in the Eq. 5. 18 and Eq. 5. 20, respectively. In Fig.5. 7 we plot the transmission spectrum for a single bus and double bus resonators

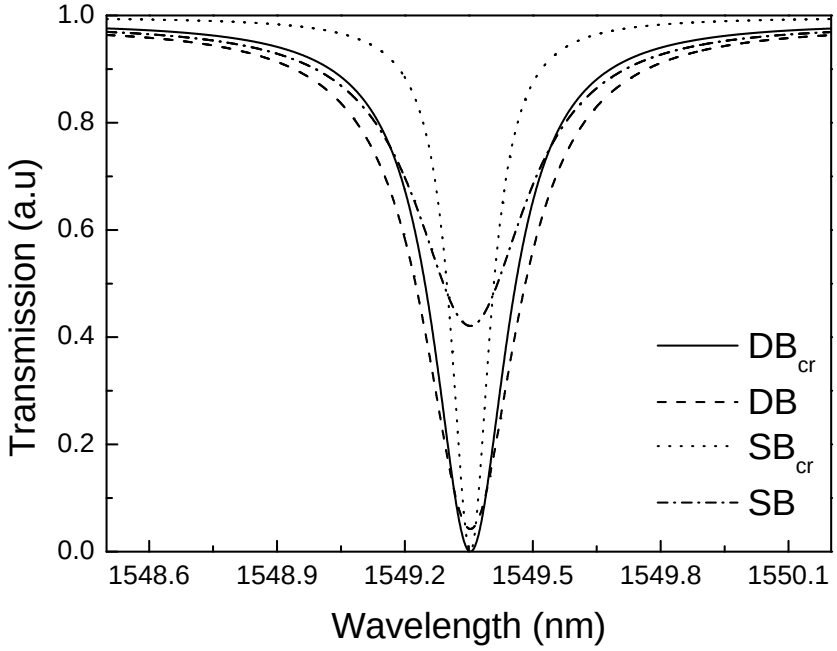

Figure 5. 7: Transmission spectrum of single bus and double bus ring resonators for both with (SB_{cr} and DB_{cr}) and without (SB and DB) critical coupling condition is achieved, respectively. The increase in steepness of the dips when critical coupling is achieved is clearly observed.

with and without critical coupling condition. Achieving the critical coupling condition, it is possible to have very high modulation depth and very narrow spectral response. Output intensity variation with cantilever displacement is given in Fig. 5. 8. It is seen that the output intensity is linear. We can write displacement and force sensitivities as

$$S_d = \frac{\Delta I_r}{I_0 \Delta z} = \beta \frac{1}{I_0} \frac{dI_r}{d\phi} \frac{d\phi}{dz} \tag{5. 28}$$

and

$$S_f = \frac{\Delta I_r}{I_0 \Delta F} = \beta \frac{1}{I_0} \frac{dI_r}{d\phi} \frac{d\phi}{dF} \tag{5. 29}$$

In Table 7.1, we compare the calculated sensitivities of the ring and race-track resonators for single bus and double bus configuration. The highest sensitivities

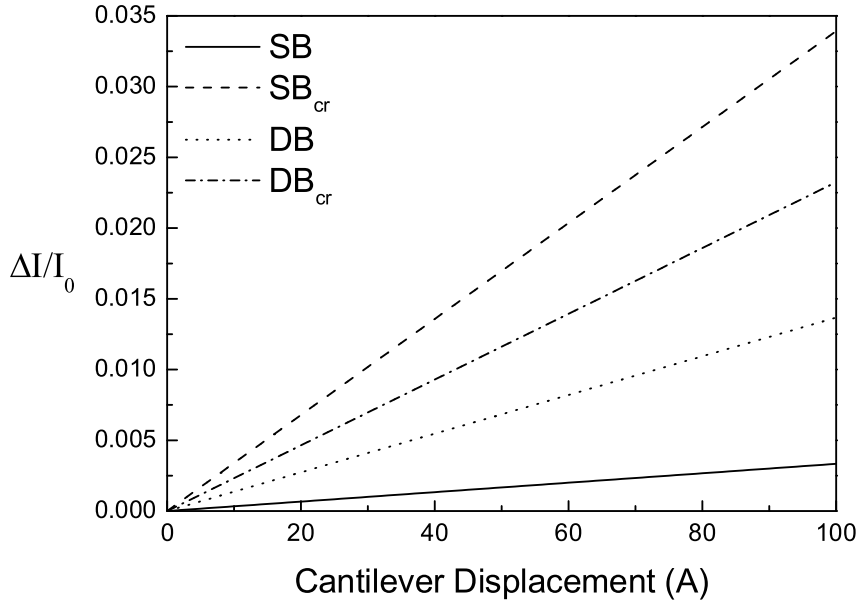

Figure 5. 8: Transmitted intensity variation with cantilever displacement for single and double bus ring resonator with (SB_{cr}, DB_{cr}) and without (SB, DB) critical coupling condition achieved. The best results are obtained under critical coupling condition.

Device	Sensitivity ($\mathring{A}^{-1}$)
SB	3.37 10^{-5}
SB_{cr}	3.39 10^{-4}
DB	1.37 10^{-4}
DB_{cr}	2.33 10^{-4}

Table 5.1: Calculated displacement sensitivities for single and double bus ring resonators with (SB_{cr}, DB_{cr}) and without (SB, DB) critical coupling.

are achieved under critical coupling conditions. The calculated sensitivities are promising, and it is possible to achieve sensitivities as high as the sensitivity of the interferometric detection. Sensitivity of the detector is depends mainly on the design of the resonator and the waveguide. Considering the round trip losses, we design the resonator to accomplish the critical coupling condition. To achieve

critical coupling, gap between straight waveguide and ring should be precisely controlled. In our design we estimate on the order of 10 dB/cm for waveguides. Under this condition, gap size for critical coupling should be of the order of 0.1 μm which can be defined by e-beam lithography but not by optical lithography. The solution for optical lithographic fabrication would be to vertically couple the ring resonator and the bus waveguide [50] , for which coupling gap can be controlled precisely through standard deposition or epitaxial growth techniques. But even if critical coupling is not achieved, the calculated sensitivities are still very good, especially for the double bus structure. In the double bus structure, the second bus can be placed next to the ring but opposite to the first waveguide and the ends of the second waveguide. The sensitivity of the ring resonator is

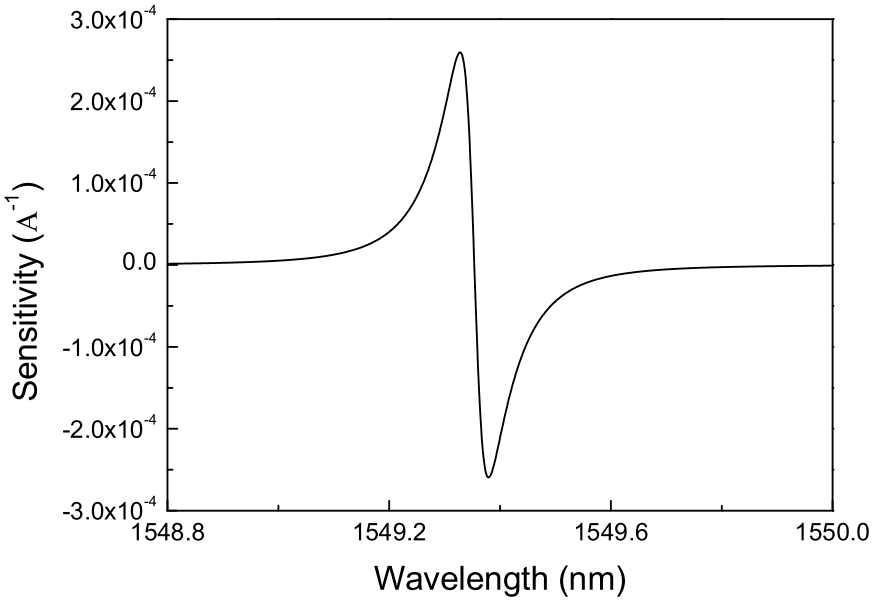

Figure 5. 9: Sensitivity vs wavelength for single bus with critical coupling achieved.

wavelength dependent. Fig. 5. 9 shows the wavelength dependence of the ring resonator. The most sensitive operation can be achieved at the wavelength which the output intensity has the steppes slope.

Chapter 6

Grating Couplers

Gratings are the one of the most important elements of optical integrated circuits. Gratings are the periodic structures with the dimensions of about wavelength of the light. Gratings are fabricated by changing the effective index of the waveguide or corrugating the waveguide surface by etching. We can categorize the grating in to main groups; passive and active gratings. Passive gratings have been used for many applications, some of them are input/output coupler, waveguide coupler deflector, focusing coupler and so on. On the other hand, periodic index modulation can be induced through acousto-optic and electro-optic effect. For these types of gratings the period can be controlled dynamically and they are called active gratings. The theory of the gratings are based on the Coupled Mode Theory (CMT). In this chapter we will introduce the use of grating coupler as displacement sensors for scanning force microscopies. Angular dependence of the coupling efficiency is used as a sensing mechanism. First, basic theory of the grating coupler will be introduce and then the application of grating to the scanning force microscopy will be discused.

6.1 Input and Output Grating Coupler

Input and output grating couplers are used to couple the guided mode to radiative fields. For the input coupler an incident beam strikes on a grating on the surface of the waveguide and due to the periodic perturbation on the surface the guided mode of the waveguide is excited by the field of the incident beam. In Figure 6.

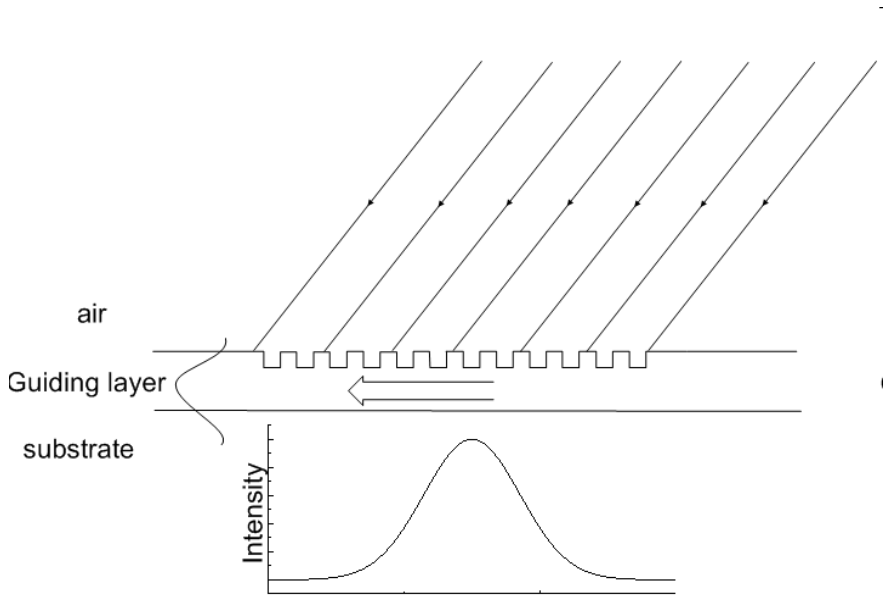

Figure 6. 1: Schematics of the input grating coupler, amplitude of the incident light is shown with a Gaussian. function

1 the schematics of the input coupler is shown. In order to excite a mode in a waveguide phase matching condition must be satisfied. Phase matching condition can be written as

$$\vec{k}_{out} = \vec{k}_{in} \pm \frac{2q\pi}{\Lambda} \tag{6. 1}$$

where $\vec{k}_{out}$ and $\vec{k}_{in}$ are the wavevectors of incident light and guided mode, respectively. Λ is the period of the grating and q is an integer number. In Figure 6. 2 k-space diagram is shown. Using Eq. 6. 1 and Figure 6. 2 we can

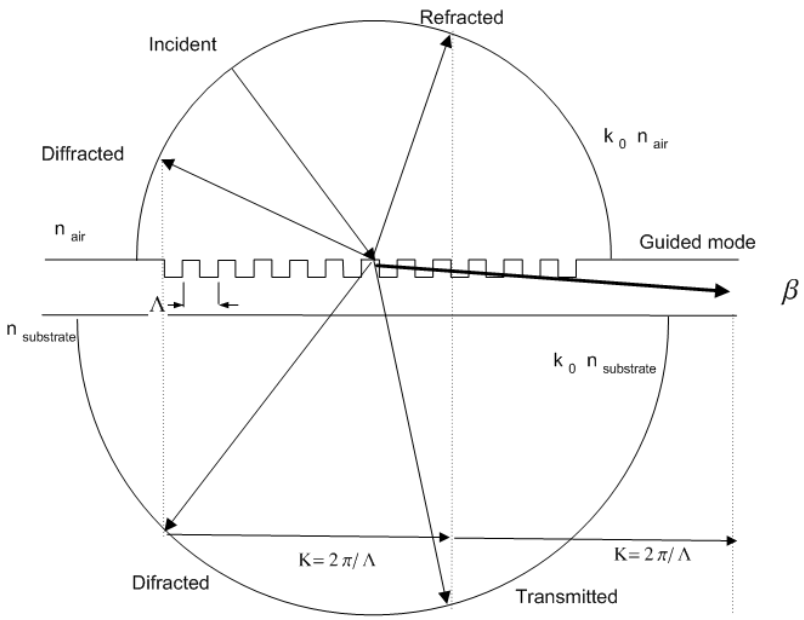

Figure 6. 2: k-space diagram of the input grating coupling diffracted, refracted and guided modes are shown.

write the coupling angle as

$$sin(\theta) = \frac{k_0 n_{air}}{\beta - qK} \tag{6. 2}$$

The most important parameter for the input coupler is the coupling efficiency. Coupling efficiency depends on the grating height, period and the coupling angle. Any deviation from the critical coupling angle changes the coupling efficiency dramatically. This sensitive behavior is used as a sensing mechanism. We can drive the angular dependence coupling efficiency using the CMT and it can be written as [51]

$$I_{coup} \propto (\frac{sin[(\beta - \beta_0)L_g]}{\pi(\beta - \beta_0)L_g})^2 \tag{6. 3}$$

where L_g is the length of the grating and β_0 is the propagation constant of the waveguide and $\beta = k_0 sin(\theta)$ and θ is the incidence angle. Figure 6. 3 illustrates the angular dependence of the grating coupler with 300 grooves and period of

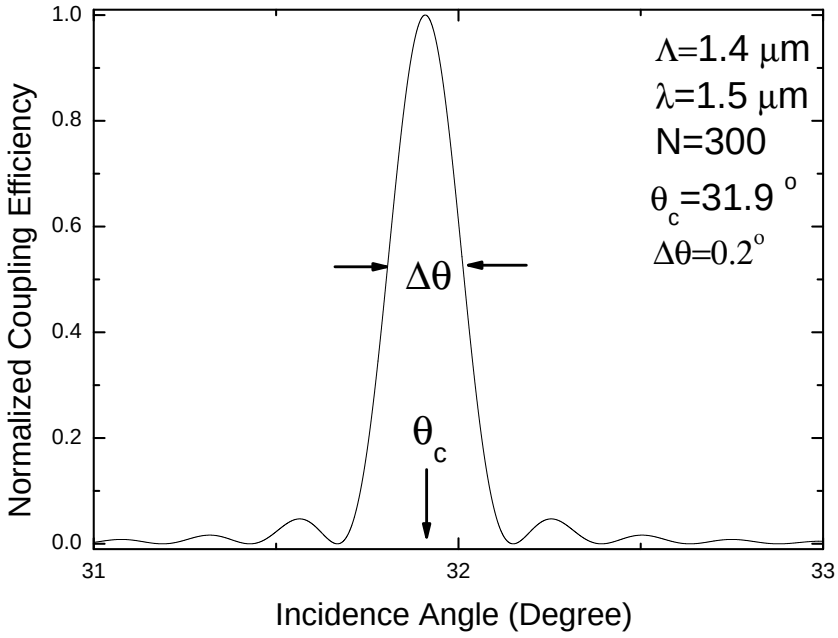

Figure 6. 3: Normalized coupling efficiency versus incidence angle for a grating coupler with 300 grooves.

1.4 μm. The width of the peak $\Delta\theta$ depends on the length of the grating and the coupling coefficient. In order to achieve high coupling efficiency incident beam diameter must be same as the grating length.

Output grating coupler couples the guided modes to the radiative modes. This means, output grating coupler coherently scatters some of the light out of the waveguide at a certain angle. The formalism of the output coupler is the same as the input coupler. Figure 6. 4 shows the schematics of the output coupler. The amplitude of the guided wave decreases exponentially along the grating. Here the incident wave is the guided mode with propagation constant of β and scattered light is the radiated directional beam. Phase matching condition can be written as

$$k_0 n_i sin(\theta) = \beta - q\frac{2\pi}{\Lambda} \tag{6. 4}$$

This condition can be satisfied in two ways, there are two radiated ray into air

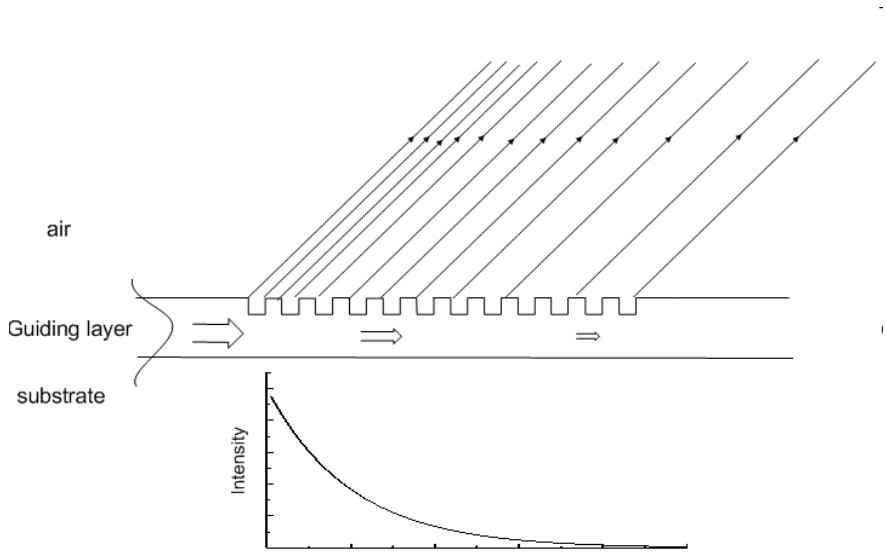

Figure 6. 4: Schematics of an output grating coupler.

and substrate. The substrate radiation introduces 50 percent loss. Figure 6. 5 represents the scattering mechanism of the output grating coupler. The coupling angle is very sensitive to the refractive index of the guiding layer and the cover material. If refractive index of the cover material changes, the coupling angle differs and measuring the coupling angle it is possible to determine the refractive index with high accuracy. This method is used as a biological and chemical sensor [53]. Absorbtion of the molecules from a liquid or gaseous medium changes the refractive index of the input grating and by monitoring the coupled light it is possible to determine the chemical ingredients.

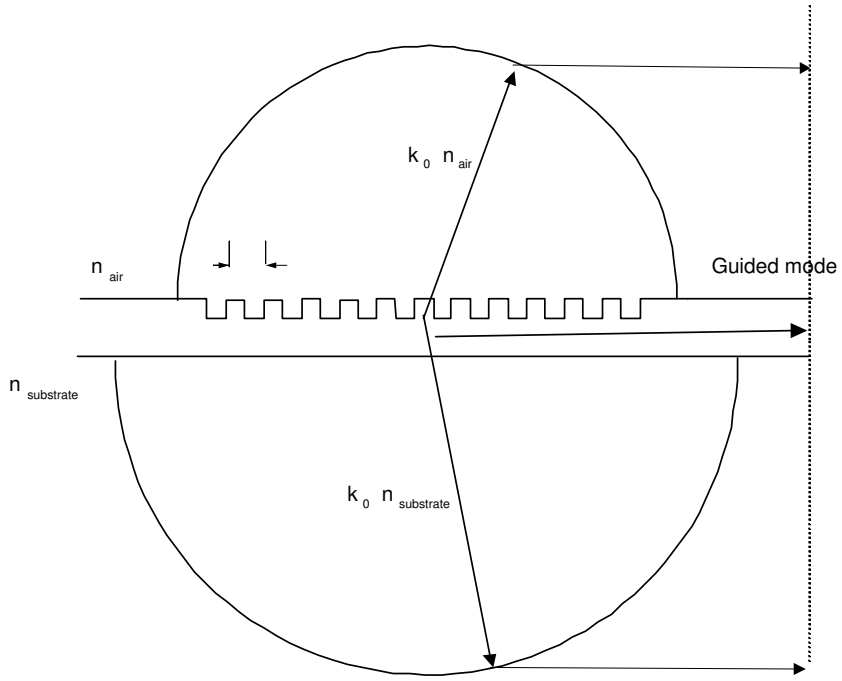

Figure 6. 5: Scattering mechanism of an output grating coupler

6.2 Input and Output Grating Coupler as a Displacement Sensor

Input and output grating couplers provide different detection mechanisms. Fig. 6. 6 shows a cantilever integrated with an input coupler. When the grating is illuminated with a laser light at the coupling angle, some of the light coupled to the waveguide and will be detected by a photodetector which can be integrated or external. For input grating coupler the most critical parameter is the coupling angle. Coupling efficiency changes dramatically with the incidence angle. Any small deviation from the coupling angle results in the change of coupling efficiency. This strong angular dependence is used to sense the cantilever displacement. Fig. 6. 7 shows the coupling efficiency as a function of the incidence angle for two gratings with lengths of 200 μm and 400 μm. The refractive index of the

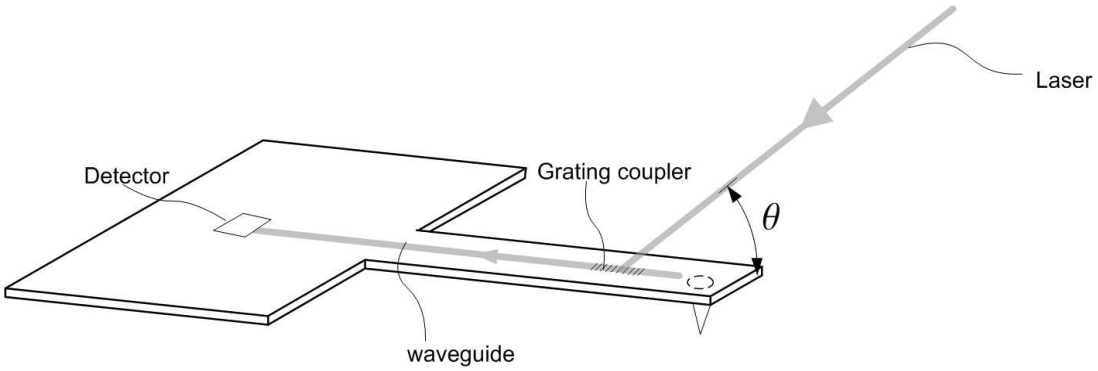

Figure 6. 6: Schematics of a cantilever integrated with an input grating coupler

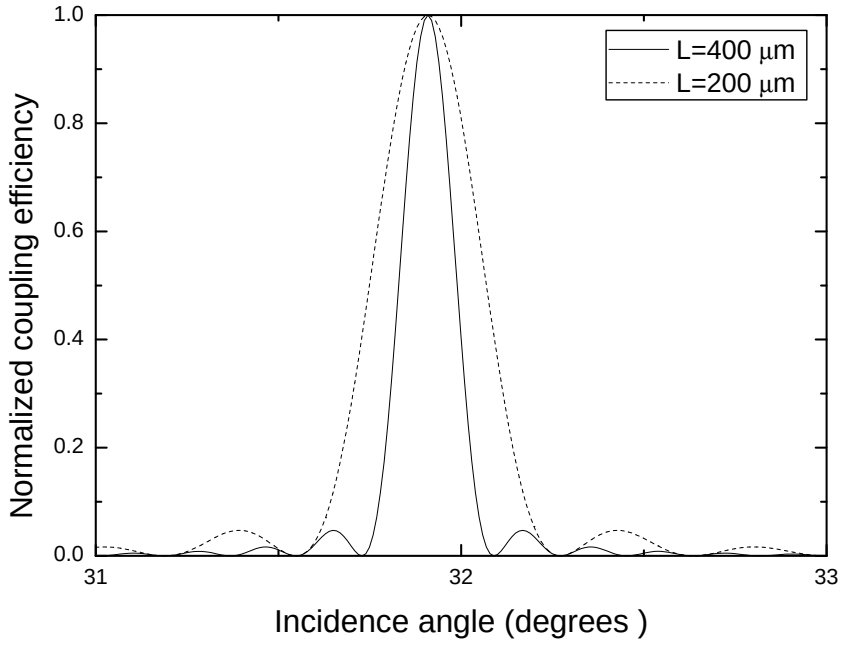

Figure 6. 7: Normalized normalized coupling efficiency vs incidence angle for gratings of length of 200 μm and 400 μm

waveguide is 1.6 and period of the grating is 1.4 μm and wavelength is 1.5 μm. The angular deviation of the coupling efficiency depends on the grating length,

tooth height and the wavelength of the light source. The grating length is limited with the cantilever length. For a cantilever with length L_{can}, for the the cantilever displacement of z, change of incidence angle can be written as

$$\Delta\theta = \frac{z}{L_{can}} \tag{6. 5}$$

in order to get high sensitivity, the angular deviation of the coupling efficiency must be comparable with the cantilever displacement. To decrease the angular deviation of the coupling efficiency, grating length must be longer, but there is a trade-off between the cantilever length and grating length. If the grating length is increased, the cantilever length must be increased which decreases the change of the incidence angle with displacement. There is an optimum value for the cantilever length. Another important parameter is the illumination angle. To get steepest slope in the output intensity with respect to cantilever displacement, grating must be illuminated at an angle different than the coupling angle which can be written as

$$\theta_{il} = \theta_c + \frac{\Delta\theta}{2} \tag{6. 6}$$

where θ_{il} is the illumination angle, θ_c is the coupling angle and $\Delta\theta$ is the angular deviation. Fig. 6. 8 depicts the normalized intensity of the coupled light as a function of the cantilever displacement. Grating length is chosen to be smaller than the cantilever length. The sensitivity is the slope of the output intensity with respect to cantilever displacement. To achieve high sensitive point the coupling angle can be tuned to get the steepest slope. For small displacements (~ 100 $\mathring{A}$) the output intensity is linear as desired.

Output grating coupler is based on the same principles with the optical lever techniques. The only difference is that output grating does not require the alignment of the laser to the cantilever which is a very tedious work. Guided light is out coupled with the grating coupler and detected with a position sensitive detector. As the cantilever displaces the intensity ratio on the detectors will change and by monitoring the output intensity with a differential amplifier the displacement can be detected. Fig. 6. 9 shows the schematics of the a cantilever integrated with a output grating coupler. The angular deviation of the scattered

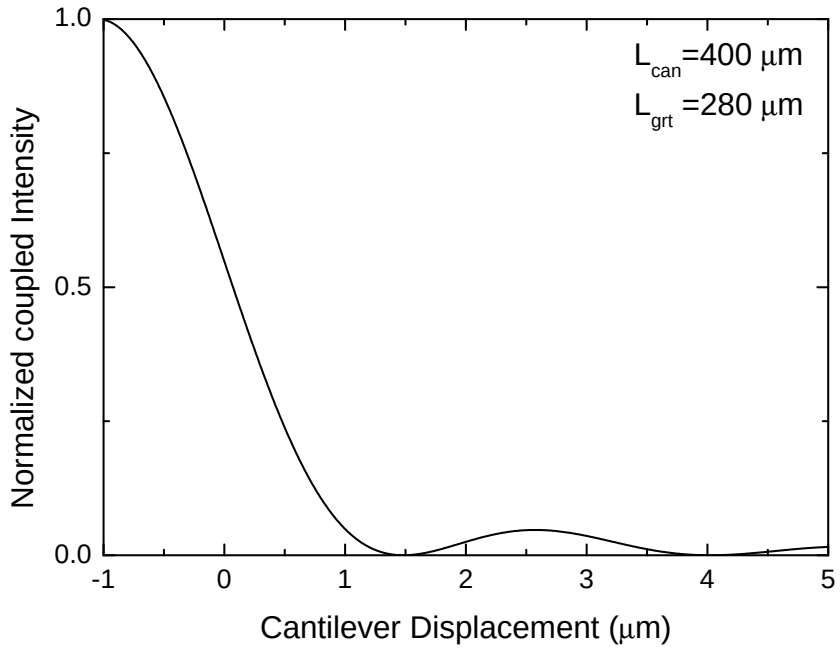

Figure 6. 8: Normalized output intensity vs cantilever displacement.

light is similar to the input grating. On the other hand, angular deviation is the same as the diffraction limited beam width of an aperture of grating length. Longer grating provides smaller angular deviation.

$$\Delta\theta \simeq \frac{\lambda}{\pi L_{grt}\cos(\theta_c)} \tag{6. 7}$$

where L_{grt} is the grating length and λ is the wavelength of the light source and θ_c is the coupling angle. Position sensitive detector must be placed far away from the cantilever. Therefore far field approximation is valid. The diffraction limited beam diameter can be written as

$$R = \frac{\lambda D}{\pi L_{grt} cos(\theta)} \tag{6. 8}$$

D is the distance from cantilever to the detector. The intensity difference of the light fall on the photodetectors can be written as

$$\Delta I = I_1 - I_2 = I\frac{3\pi L_{grt} cos(\theta)}{\lambda L_{can}} z \tag{6. 9}$$

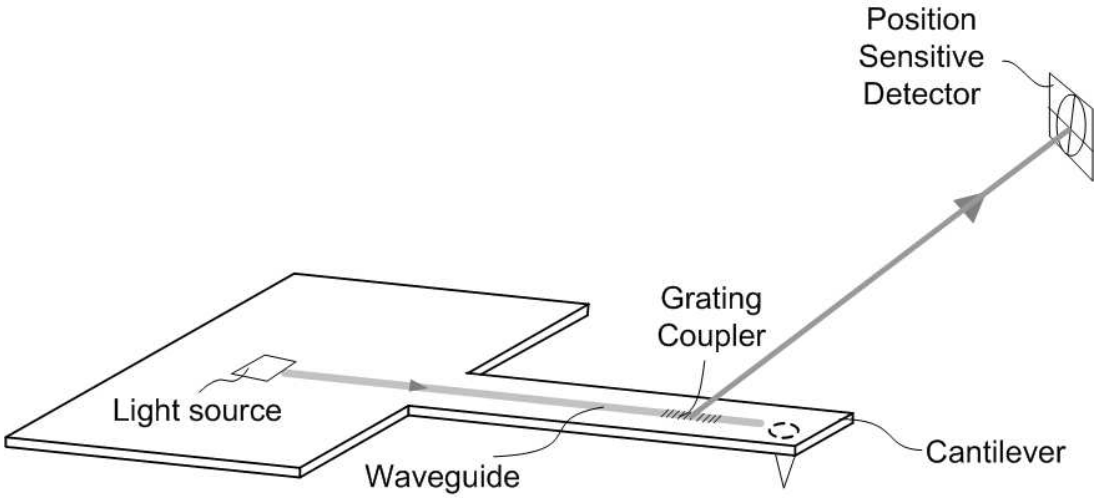

Figure 6. 9: Schematics of a cantilever integrated with an output grating coupler

From Eq. 6. 9 the intensity change on the photodetectors are independent of the distance unless the detectors are in the near field of the cantilever. The advantage of this method is that the alignment is very simple compared to the optical lever technique. In this novel method, only the the detector alignment is required and there is no need to align laser light which provides very compact and stable scanning force microscope.

Chapter 7

Noise Analysis

The resolution of scanning force microscope is limited by the noise of the system [54, 55]. The minimum detectable distance (MDD) depends on not only the sensitivity but also the noise of the microscope. Noise level of the system establishes the minimum detectable optical power on the photodetector necessary to obtain the cantilever displacement. In this chapter, we will study the fundamental noise sources for integrated optical displacement sensors. Finally we will compare the MDD for all integrated optical sensors that described in the previous chapters. Integrated optical displacement method consist of four main parts; laser source, integrated optical device, cantilever, and the photodetector. All these parts introduce different noises to the system. Noise is an additive quantity and in order to calculate the noise of the all system we have to add all the contributions. Some contributions can be eliminated using proper experimental design, but some of them are fundamental and can not be eliminated. Detection methods also affect the noise level. Scanning force microscope has two operating modes; continuous measurement (DC) and periodic measurement (AC). In the AC mode, cantilever is driven near its resonance frequency and the the output of the photodetector is detected with a lock-in amplifier and provide a detection bandwidth. In this mode, some of the noises can be eliminated and the MDD is limited with the fundamental noises such as shot noise and Johnson noise. Displacement sensitivity is defined as the variation of the normalized output

intensity per unit displacement of the tip. It can be written as

$$S = \frac{\Delta I}{I_0 \Delta z} \tag{7. 1}$$

The input intensity (power), I_0, depends on the lights source and typically is of the order of mW's. Photodetector converts the optical power to the electrical signal and this signal is amplified with a low loss amplifier. What we can measure is the current on the photodetector, i. It can be written as

$$i = RI \tag{7. 2}$$

where R is the responsivity of the detector and I is the optical power. The performance of the optical detector is characterized by the signal to noise ratio (SNR) which is defined as

$$SNR = \frac{average\ signal\ power}{noise\ power} \tag{7. 3}$$

Minimum detectable distance (MDD) is defined as the distance in which the SNR is unity and

$$S = \frac{i_{noise}}{I_0\ MDD} \tag{7. 4}$$

and

$$MDD = \frac{i_{noise}}{I_0\ S} \tag{7. 5}$$

where S is the sensitivity. We will now discus the noise contributions in detail.

7.1 Laser Noise

Not only the output intensity but also the phase and the frequency of a semiconductor laser fluctuate in time. There are two fundamental mechanism that produce these fluctuations; electron-hole recombination and spontaneous emission. The cantilever displacement is measured directly from the intensity changes therefore we have to estimate the magnitudes of these fluctuations (noises). For a semiconductor laser, the noise is given as the relative intensity noise (RIN)

$$RIN = \frac{(\delta P)^2}{P^2} \tag{7. 6}$$

and we can write $SNR = 1/RIN$. This noise exist for all types of integrated optical devices employed to detect cantilever displacement in this work. The laser intensity variation can be eliminated by introducing a reference photodetector and using a differential amplifier, the output intensity can be normalized. For our design we choose a tunable laser source which provides higher intensity and wavelength stability [57] . This laser provides 0.01 dB long-term intensity stability which means %0.1 power variation. Another important noise is the random wavelength variation. For ring resonator and Bragg grating displacement sensors the wavelength variation causes output intensity variation. In order to reduce this noise we have to use a laser which provides high wavelength stability. Tunable laser Source (TLS 8800) has 0.1 pm wavelength stability which introduce %0.01 intensity variation. On the other hand Mach-Zehnder interferometers and Michelson interferometers are broad band devices which means wavelength variation does not cause intensity variation. For a grating coupler, coupling angle is given as

$$sin(\theta) = n_w - \frac{\lambda}{\Lambda} \tag{7. 7}$$

and the variation of the coupling angle is

$$\Delta\theta = \frac{\Delta\lambda}{\Lambda} \tag{7. 8}$$

which results in $\Delta\theta = 10^{-7} degree$ which can be neglected. The intensity variation and wavelength variation can be reduced by using suitable light sources and lock-in amplifiers. These are not fundamental noises and can be eliminated with proper design. There is also another noise which is called laser pointing noise. Laser pointing noise is due to the mechanical vibration of the laser. Unlike the other optical detection methods, the integrated optical detection avoids this noise. Laser is butt coupled to the substrate and pointing noise is eliminated. This noise can be effective only in the grating coupler which requires a laser focused on the grating coupler.

7.2 Cantilever Noise

The main noise source due to the cantilever is the thermal vibration of the cantilever. There are also noises due to the vibrating bimorph. To analyze the thermal vibrational noise, we assume the cantilever as simple harmonic oscillator. At finite temperatures, the cantilever vibrates due to thermal excitation. The cantilever is subject to a random time-dependent Brownian motion around its equilibrium position [56]. The thermal mechanical noise of the cantilever is estimated as

$$\Delta z_{thermal} = \sqrt{\frac{2k_bTB}{\pi Qkf_0}} \tag{7. 9}$$

where k_b is the Boltzman constant, T is the temperature, B is the band-width, Q is the quality factor of the cantilever, k is the spring constant and f_0 is the resonance frequency of the cantilever. We choose a rectangular cantilever with length of 200 μm width of 50 μm and thickness of 5 μm. The resonance frequency is 50 kHz, the spring constant is 16 N/m and the band-width is about 1 kHz. The quality factor of the cantilever $Q = 100$ is chosen for analysis. At room temperature, the thermal vibrational noise is obtained as $\Delta z_{thermal} = 0.0017$ $\mathring{A}$ which is very small compared to the shot noise. Fig. 7. 1 shows the calculated thermal vibrational noise amplitude. As the length of the cantilever increases the spring constant decreases and the vibrational noise increases.

7.3 Detector Noise

There are two fundamental noises for photodetectors; shot noise and thermal noise. These noises are fundamental noises and they can not be eliminated. Shot noise is a fundamental noise that exist in all optical detection processes. When the optical power is detected photons fall randomly on the detector and time average of the received power fluctuates due to the this randomness. Origin of this noise is the quantum nature of photons and there is no way to avoid it. The generated photo current on the detector is

$$i = RI \tag{7. 10}$$

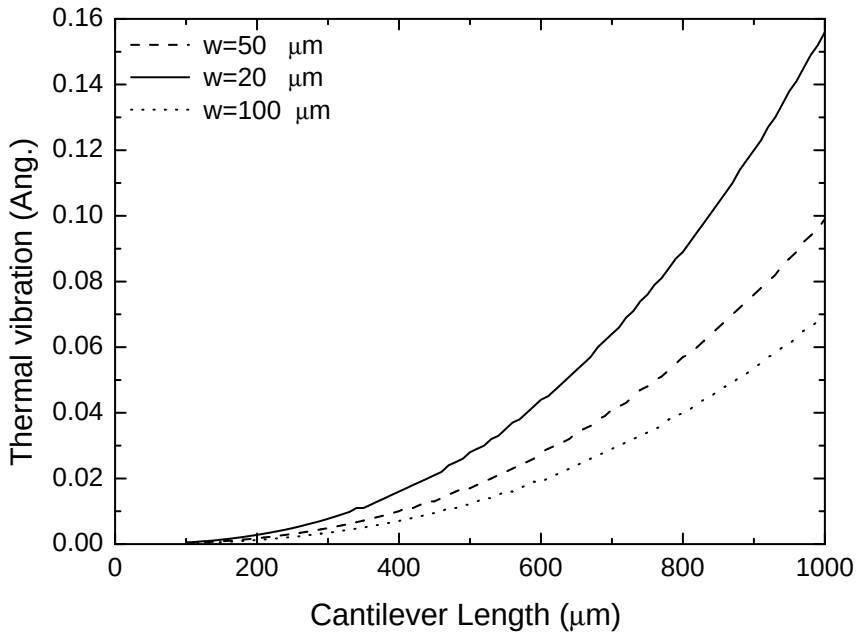

Figure 7. 1: Calculated thermal vibration as a function of the cantilever length for different cantilever widths.

where R is the responsivity and I is the received optical power. Shot noise can be written as

$$i_{shot} = \sqrt{2eiB} \tag{7. 11}$$

where e is the electron charge and B is the bandwidth. SNR can be written as

$$SNR = \frac{i}{i_{shot}} = \sqrt{\frac{i}{2eB}} \tag{7. 12}$$

SNR increases with the received power. For 100 μW optical power the shot noise current is $\Delta i = 6\ 10^{-10} A$, SNR is 10^5 and shot noise limited MDD is 0.027 $\mathring{A}$. Another interesting property of shot noise is that it has constant spectral density which means independent of frequency. Due to this property, shot noise is also called as *white noise*. Another noise source for photodetectors is the thermal noise. At finite temperature electrons in a conductor move randomly. Random

Device	Sensitivity ($\mathring{A}^{-1}$)	MDD (Å)
Mach-Zehnder	6.9 10^{-5}	0.077
Ring Resonator	3.39 10^{-4}	0.016
Grating input coupler	1.2 10^{-4}	0.044

Table 7.1: Calculated displacement sensitivities and shot noise limited minimum detectable distances for $100\mu W$ optical power and 1 kHz band width.

thermal motion of the electrons in a resistor produce a fluctuating current.

$$i_{thermal} = \sqrt{\frac{4kTB}{R}} \tag{7. 13}$$

where k is the Boltzman constant, T is the temperature and R is the resistance. If the received power is high enough (mW's) the dominant noise is the shot noise and it determines the noise level of the system. Generally for all scanning force microscopes which use optical detection the dominant noise source is the shot noise. For 100 μW optical power, shot noise limited MDD is 0.027 $\mathring{A}$. SNR can be increased by increasing the optical power. Cantilever vibrates with very small amplitudes (100 $\mathring{A}$) therefore the interferometer must be biased such that at equilibrium position the optical power must be large enough to get high SNR. Mach-Zehnder interferometer can be biased introducing a path difference between the two arms. Ring resonators and Bragg grating can be biased by tuning the wavelength of the laser such that the output is half of the maximum power at equilibrium. Grating couplers can also be biased by changing the coupling angle to get half of the output power at the equilibrium. It should also be mentioned that, for each device, there exists a configuration which provides the most sensitive operation and for all this configuration SNR is higher than the optical lever techniques. The linearity of the output power is another desired property. All described sensors are linear about the equilibrium position. Mach-Zehnder interferometer is linear over a large range. Sensitivity of the sensor is the slope of the output signal therefore linear output provides constant sensitivity.

Chapter 8

Conclusions and Suggestions

In this thesis, we have studied the use of integrated optical waveguide devices acting as integrated displacement sensors on cantilevers for scanning force microscopes. These displacement sensors include integrated optical waveguide devices such as Mach-Zehnder interferometer, Bragg gratings, ring resonators, race track resonators and grating input/output couplers fabricated on a cantilever to measure the displacement of the tip due to the forces between surface and the tip. The displacement of the cantilever tip is measured directly from the change of the transmission characteristics of the optical device. As the tip displaces, the stress on the cantilever surface changes the refractive index of the materials that make up the integrated optical device which cause variations in its optical transmission characteristics. We have also studied an optical waveguide grating coupler fabricated on the cantilever for the same purpose. In two different embodiments of this device, light is either coupled in or out of the waveguide via the waveguide grating coupler. The displacement of the cantilever alters the direction of the scattered light and measuring the power of the scattered light with a position sensitive detector allows for the detection of tip displacement. In both embodiments of this optical sensors, it is possible to determine the cantilever displacement with high sensitivity without tedious alignment. The minimum detectable distance of the detectors are limited by the shot noise.

A further application of this novel optical sensor can be made for use in

arrays of displacement sensors. Both one and two dimensional arrays of the integrated optical devices acting as sensors on cantilevers are possible to increase the throughput of these devices. Fig. 8. 1 shows the one dimensional cantilever

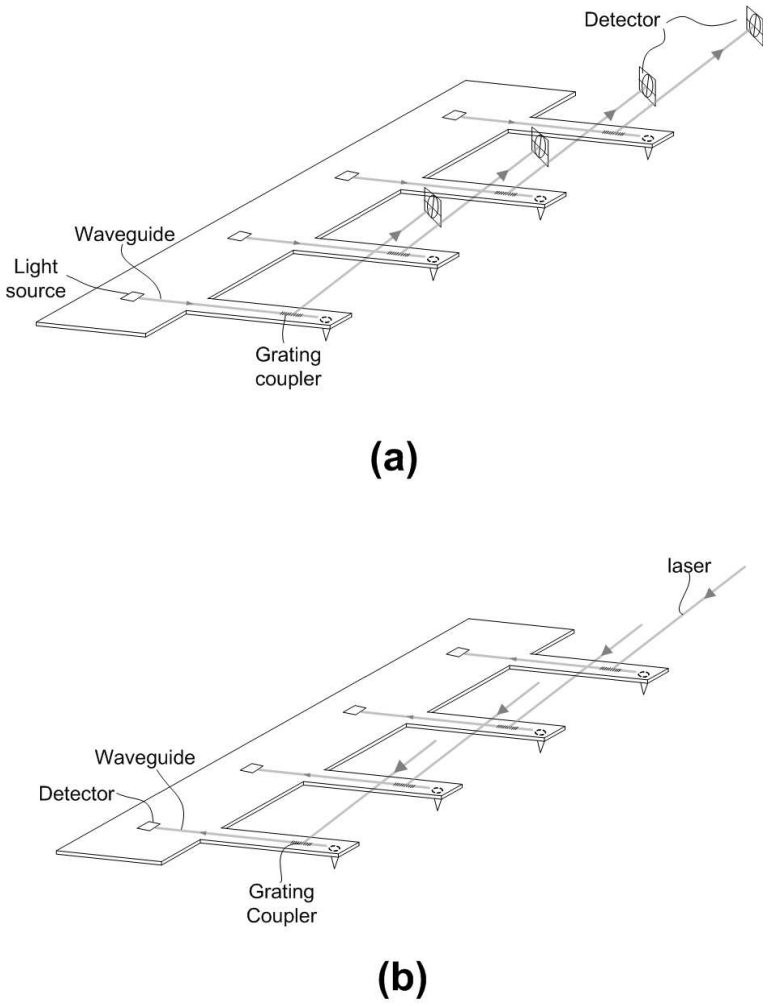

Figure 8. 1: 1D array of cantilever integrated with grating output coupler (a) and input coupler (b).

arrays integrated with a grating coupler. In Fig. 8. 1 a one dimensional grating output couplers integrated on the cantilevers are shown. Integrated or external light sources are used to couple the light to the waveguide and grating coupler

is used to out couple some of the light to be detected with position sensitive detector. The same configuration can be made for input coupler grating and Fig. 8. 1 b shows this configuration. Cantilever array is illuminated with a collimated laser beam and coupled light for each cantilever is detected with an integrated detector.

We have proposed several novel types of integrated displacement sensors and we have shown the feasibility of these sensors. Mach-Zehnder interferometer is the most simple and promising device. First experimental work must be done on this device. The sensitivity is a bit smaller than the others, on the other hand the output intensity is linear over a long range and it is a broad band interferometer which is immune to wavelength variation of the light source. The most sensitive proposed displacement sensor is the ring resonator. The dimension of the ring resonator is very small which makes the fabrication harder, but it can be fabricated using optical lithography. Grating coupler is also very promising. The grating structure can be fabricate using optical lithography which makes the fabrication very easy.

Bibliography

[1] G. Binning, H. Rohrer, Ch. Gerber, E. Weibel "Atomic Force Microscope", Phys. Rev. Lett. , **49**, 57, (1982).

[2] G. Binning, C.F. Quate , Ch. Gerber "Atomic Force Microscope",Phys. Rev. Lett. , **56**, 930, (1986).

[3] C.Mathew Mare, Gary M. McClelland, Ragnar Erlandsson Shirley Chiang "Atomic Scale Friction of Tungsten Tip an Graphite Surface",Phys. Rev. Lett. , **59**, 1942, (1987).

[4] Y. Martin, H.K. Wickramasinghe, Appl. Phys. Lett., **50**, 1455, (1987).

[5] E.A. Ash, G. Nicholls, Nature, **237**, 510, (1972).

[6] M. Tortonese "Cantilevers and Tips for Atomic Force Microscopy", IEEE Engineering in Medicine and Biology, , **28**, (1997).

[7] D. Sarid "Scanning Force Microscopy", Oxford University Press, New Yok, (1994).

[8] Gerhard Meyer, M. Nabil "Novel Optical approach to atomic force microscopy", Appl. Phys. Lett., **53** 1045, (1988).

[9] P.K. Hansma, B. Drake, D. Grigg, C.B. Prater, F. Yashar, G. Gurley, V. Elings, S. Feinstein, "A new, optical-lever based atomic force microscope", Appl. Phys. Lett., **76** 796, (1994).

[10] R. Erlandsson G.M McClelland, C.M. Mate, S. Chiang, "Atomic Force Microscopy using optical interferometer", J. Vac. Sci. Technol. A , **6** 266, (1988).

[11] D. Rugar, H.J. Mamin, R. Erlandsson , J.E. Stern, B.D. Terris "Force microscope using a fiber-optic displacement sensor", Rev. Sci. Instrum. , **59** 2337, (1988).

[12] D. Rugar, H.J. Mamin, P. Guethner "Improved fiber-optic interferometer for atomic force microscopy", Appl. Phys. Lett., **55** 2588, (1989).

[13] S.R. Manalis, S.C. Minne, A. Atalar, C.F. Quate "Interdigital cantilevers for atomic force microscopy", Appl. Phys. Lett., **69** 3944, (1996).

[14] G. Yaralioglu, A. Atalar, S.R. Manalis, C.F. Quate "Analysis and design of an interdigital cantilevers as a displacement sensor", J. Appl. Phys., **83** 7405, (1998).

[15] M. Totonose, R.C. Barrett, C. F.Quate "Atomic Resolution with an atomic force microscope using piezoresistive detection", Appl. Phys. Lett., **62** 834, (1993).

[16] S.C Minne , S.R. Manalis, A. Atalar , C.F. Quate. "Contact imaging in atomic force microscope using a higher order flexural mode combined with a new sensor", Appl. Phys. Lett., **68** 1427,(1996).

[17] Terunobu Akiyama, Andreas Tonin, Hans-Rudolf hidber,Jurgen Brugger, Peter Vettiger, Urs Staufer , Nico F. de Rooij "Characterization of an integrated force sensor based on a MOS transistor for application in scanning force microscopy", Sensors and Actuators A, **64** 1, (1998).

[18] T. Goddenhenrich, H. Lemke , U. Hartmann, C. Heiden "Force microscope with capacitive displacement detection", J. Vac. Sci. Technol. A, **8** 383,(1990).

[19] N. Blanc, J. Brugger, N.F. de Rooij, U. Durig "Scanning Force microscopy in the dynamic mode using microfabricated capacitive sensor", J. Vac. Sci. Technol. A, **8** 383,(1990).

[20] C. Wagner, J. Frankenberger, P. P. Daimel "Optical pressure sensor based on Mach-Zehnder interferometer integrated with a lateral a-Si:H p-i-n photodiode," IEEE Electronic Device Letters **10**, 1257, (1993)

[21] Masayuki Izutsu, Akira Enokihara, Tadasi Sueta "Integrated Optic Temperature and Temperature and Humidity Sensor ," IEEE J. Lightwave Tech. **7**, 833, (1986)

[22] Torben Storgaard-Larsen , Siebe Bouwstra , Otto Leistiko "Opto-mechanical accelerometer based on strain sensing by Bragg grating in planar waveguide," Sensors and Actuators A **52**, 25, (1996)

[23] B. J. Luff, R. D. Harris, J. S. Wilkinson, R. Wilson,D. J. Schiffirin "Integrated-optical directional coupler biosensor," Optics Letters **21**, 618, (1996)

[24] G. N. De Brabander, J. T. Boyd, G Beheim "Integrated optical ring resonator with micromechanical diaphragm for pressure sensing," IEEE Photonics Tech. Lett. **6**, 671, (1994)

[25] Clifford Pollock, "Fundamentals of Optoelectronics" Richard D. IRWIN INC. 1995 USA

[26] Katsunari Okamoto, "Fundamentals of Optical Waveguides" Akademic Press 2000 USA

[27] BeamPROPE, "RSoft. Inc." Colunbia University. USA

[28] BeamPROPE Manual, "RSoft. Inc." Colunbia University USA.

[29] T. S. Narasimhamurty , "Photoelastic and Elecro-Optic Properties of Crystals" Plenum Press 1981 New York.

[30] A. Ghatak, K. Thyagarajan , "Optical Electronic" Cambridge University Press 1989 Cambridge

[31] Saeed Moaveni, "Finite Elemnt Analysis" Prentice Hall, 1999 New Jersey

[32] Melle S M, Liu K, Measures M ,1992 IEEE Photonic Technology Letters, **4** 516, (1992)

[33] Youlong Y, Hwayaw T, Wenghong C,Demokan M S, Optic Letters, **25** 1141, (2000)

[34] Yariv A, Winsor H V, Optic Letters, **5** 87, (1980)

[35] Ferreira L A, Diatzikis E V, Moreira P J, Santos J L, Farahi F , Optical Fiber Technology, **6** 365, (2000)

[36] Bashir R, Gupta A, Neudeck G W, McElfresh M and Gones R, J. Micromech. Microeng. **10** 483, (2000)

[37] Hansen O, Boisen A, Nanotechnology, **10** 51, (1999)

[38] Streifer W, Scifres D R, Burham R D , IEEE Quantum Electron., **11** 867, (1975)

[39] Haus H A, Schmidt R V 1977 *IEEE Trans. Sonic Ultrason* **SU-24** 94

[40] M. Kohtoku, S. Oku, Y. Kadota, Y. Shibata, and Y. Yoshikuni, " 200-GHz FSR periodic multi-demultiplexer with flattened transmission and rejection band by using a mach-zehnder interferometer with a ring resonator," IEEE Photonics Tech. Lett. **12**, 1174, (2000)

[41] B. E. Little, J. S. Foresi, G. Steinmeyer, E. R. Thoen, S. T. Chu, H. A. Haus, E. P. Ippen, L. C. Kimerling, and W. Greene, " Ultra-compact Si-SiO2 microring resonator optical channel dropping filters, " IEEE Photonics Tech. Lett. **10**, 549, (1998)

[42] B. E. Little, H. A. Haus, J. S. Foresi, L. C. Kimerling, E. P. Ippen, and D. J. Ripin, " Wevelength switching and routing using absorption and resonance, " IEEE Photonics Tech. Lett. **10**, 816, (1998)

[43] J. M. Choi, R. K. Lee, and A. Yariv "Control of critical coupling in a ring resonator-fiber configuration: application to wavelength-selective switching, modulation, amplification, and oscilation, " Optic Letters **26**,1236, (2001)

[44] J. L. Altman *Microwave Circuits*, Princeton, N. J., Van Nostrand, (1964)

[45] M. K. Chin, and S. T. Ho "Design and Modeling of waveguide-coupled single-mode microring resonators, " Journal of Lightwave Technology **16**,1433 (1998)

[46] S. Kim, and A. Gopinath "Vector analysis of optical dielectric waveguide bends using finite-difference method, " Journal of Lightwave Technology **14**,2085 (1998)

[47] E. C. M. Pennings, R. J. Deri, and R. J. Hawkins "Simple method for estimating usable bend radii of deeply etched optical rib waveguides, " Electronics Letters **27**, 1532, (1991)

[48] M. Tortonese, "Cantilevers and tips for atomic force microscopy," IEEE Engineering in Medicine and Biology, 28, (1997)

[49] A. J. Brook, S. J. Bending, J. Pinto, A. Oral, D. Ritchie, H. Beere, A. Springthorpe, M.Henini, "Micromachined III-V cantilevers for AFM-tracking scanning hall probe microscopy," J. Micromech. Microeng. **13**, 124, (2003)

[50] B. E. Little, S. T. Chu, W. Pan, D. Ripin, T. Kaneko, Y. Kokubun and E. Ippen, " Vertically coupled glass microring resonator channel droping filters, " IEEE Photonics Tech. Lett. **11**, 215, (1999)

[51] Kinichiro Ogava, William S. C. Chang, Bhushan L. Sopori, Pred J. Rosenbaun“ A Theoretical Analysis of Etched Grating Coupler for Integrated Optics ” IEEE J. Quantum Electronics **9**, 29, (1973)

[52] J. H. Harris, R. K. Winn, D. G. Dalgoutte“ Theory and Design of Periodic Couplers” Applied Optics **11**, 2234, (1972)

[53] K. Tiefenthaler, “ Sensitivity of grating coupler as integrated-optical chemical sensor” J. Opt. Soc. Am. B **6**, 2, pp. 209, (1989)

[54] O. Hansen, A. Boisen, “Noise in piezoresistive atomic force microscopy,” Nanotechnology. **10**, pp. 51, (1999)

[55] D. P. E. Smith, “Limits of force microscopy,” Rew. Sci. Instrum. **66** 5, 3191, (1999)

[56] S. Rast, C. Wattinger, U. Gysin, E. Meyer “The Noise of cantilever,” Nanotechology **11** pp. 169, (2000)

[57] ILX Lightwave Corp. *Tunable laser Source TLS 8800 Series*

[58] Govind Agrawal, “Fiber Optic Communication System,” John Wiley & Sons, INC. 1999, Canada